A Note on Hypoelastic Models: A Benchmark-Oriented FEM Lagrangian Formulation in FeniCSx

Bastien Sauty, Claire Morin, Stéphane Avril, Michele Marino

A Note on Hypoelastic Models: A Benchmark-Oriented FEM Lagrangian Formulation in FeniCSx

Bastien Sauty[1,2], Claire Morin[2], Stéphane Avril[2], Michele Marino[1*]

[1*]Multiscale and Multiphysics Mechanics Group (M2M), Department of Civil Engineering and Computer Science Engineering, University of Rome Tor Vergata, Rome, Italy.
[2]Mines Saint-Etienne, INSERM, U1059 SAINBIOSE, Saint-Etienne, France.

*Corresponding author(s). E-mail(s): m.marino@ing.uniroma2.it;
Contributing authors: bastien.sauty@emse.fr; claire.morin@emse.fr; avril@emse.fr;

Abstract

Hypoelastic formulations are commonly used for modeling materials undergoing large elastic deformations. Yet their lack of an underlying energy potential raises concerns about integrability and energy consistency. This work addresses the longstanding gap between the theoretical notion of integrability and its numerical realization in finite element implementations. We develop a total Lagrangian framework for hypoelasticity and implement it within the open-source FEniCSx platform, enabling direct comparison of various objective stress rates. Two stress-integration algorithms, namely a forward Euler and an implicit midpoint, are formulated and compared, together with a sub-iterative variant to enhance accuracy. The framework is tested through benchmark problems involving cyclic and non-proportional shear loading. We systematically assess the interplay between constitutive rate choice and numerical integration accuracy. The results confirm that classical Jaumann and Green–Naghdi stress rates are non-integrable for grade-zero hypoelasticity, producing residual stresses and spurious energy accumulation. Conversely, the logarithmic rate preserves path independence for grade-zero hypoelasticity. Moreover, we show that even theoretically integrable models can exhibit numerical non-integrability when discretized inconsistently. Finally, the framework is applied to a non-grade-zero hypoelastic model featuring

a non-constant stiffness matrix derived from the Exponentiated Hencky energy, assessing its numerical integrability and performance. The proposed framework provides a transparent, extensible basis for evaluating hypoelastic models in boundary value problems, bridging theoretical consistency and computational practice. This supports the development of integrable constitutive formulations for large-deformation mechanics.

Keywords: Hypoelasticity, FEM, FeniCSx, Integrability

1 Introduction

Hypoelastic formulations are commonly used to model the elastic part of materials undergoing large deformations, particularly within frameworks where inelastic behaviors are the primary focus, such as geomechanics, metal forming, and soft tissue mechanics [1–6]. These models define the stress response via rate equations instead of a stored energy function, making them particularly suitable for applications based on material tangent response descriptions [7]. Traditionally, hypoelastic formulations prioritize compatibility with Eulerian or updated Lagrangian schemes [8]. Objectivity – i.e., frame indifference under rigid body motions – is a critical requirement in these formulations and it is enforced using objective stress rates such as the Jaumann, Green–Naghdi, or Oldroyd rates [9].

A prominent application of hypoelasticity is in multiscale modeling, where the macroscopic material behavior is informed by structural responses of their microstructure [3, 10–13]. In such frameworks, the tangent material stiffness is obtained from analytical or numerical solutions of the mechanical response at lower-scale and is explicitly integrated into a macroscopic constitutive law, often without an underlying energy potential [14]. Hypoelastic models are particularly convenient in this setting because they allow for direct implementation of tangent stiffness updates while maintaining compatibility with numerical solvers [15]. This makes them also attractive for capturing nonlinear or history-dependent behaviors emerging from complex microstructural responses – even when a clear energetic potential is difficult to define. However, the lack of an energy potential in the macroscopic model can raise concerns about consistency, particularly in cyclic loading or inelastic mechanisms [16].

A central issue in hypoelasticity is integrability – whether the stress response derives from a potential, making it path-independent and conservative. Integrability ensures that mechanical work depends only on the current strain state and not on the deformation path. This distinction was first addressed by Bernstein [17], who defined integrability as a criterion for hypoelastic models to correspond to a well-defined strain energy potential. If a hypoelastic model is integrable, it can be considered Green-elastic and therefore, equivalent to a hyperelastic formulation [18]. In contrast, non-integrable models may generate spurious energy under cyclic loading, violating thermodynamic consistency [19, 20]. This issue is also especially problematic when hypoelastic models are used to describe the elastic part of inelastic (e.g., elastoplastic) behavior. While inelasticity is inherently path-dependent, the elastic response should

remain path-independent to ensure meaningful return mapping. Failure to guarantee this can result in artificial energy dissipation and incorrect stress predictions [21–23]. This issue becomes particularly critical under finite shear and cyclic loading, where non-integrable rates can lead to closed stress–strain loops that accumulate positive work [24–26]. Despite these limitations, hypoelastic models continue to be widely used due to their computational simplicity and ease of implementation [16].

Most commonly used rates – such as the Zaremba–Jaumann and Green–Naghdi derivatives – fail to satisfy the integrability conditions, even for the simplest case of constant stiffness, that is grade-zero hypoelasticity [27–29]. The notable exception is the logarithmic rate, which has been shown to be integrable in this case [30–33]. Recently, Jiao and Fish [22, 23] demonstrated that the logarithmic rate fails to satisfy integrability conditions when plastic residual stresses are present. To address this, they proposed a kinetic logarithmic rate capable of restoring integrability [34]. However, despite being integrable and energetically consistent, both the standard logarithmic rate (in elastic regimes) and the kinetic logarithmic rate (in plastic regimes) remain largely overlooked by the computational community [16]. This is primarily due to the significant theoretical and numerical complexities involved in their implementation.

Moreover, a critical but often underexplored distinction exists between theoretical and numerical integrability. While theoretical integrability involves the existence of a strain energy function satisfying mathematical conditions, numerical integrability concerns the discrete behavior of the model in its computational setting. A theoretically integrable model may fail to exhibit path-independent stress updates in numerical implementations if inappropriate stress rates or integration schemes are used [35]. This gap becomes more pronounced in commercial finite element software such as Abaqus, LS-DYNA and ANSYS, which typically embed non-integrable hypoelastic frameworks formulated via objective rates such as the Jaumann or Green-Naghdi derivatives. These codes rarely provide mechanisms to assess whether the discrete evolution of stress preserves integrability.

Furthermore, Eulerian and updated Lagrangian (UL) formulations, often used for hypoelastic modeling, introduce their own challenges. Eulerian frames struggle with tracking material history, while UL schemes – though a compromise – may suffer from mesh dependency due to cumulative geometric errors, evolving reference frames and numerical instabilities [36–38]. These numerical artifacts can conceal or exaggerate integrability violations, further complicating the assessment of physical fidelity. In contrast, a total Lagrangian formulation provides a fixed reference configuration that facilitates consistent tracking of material states and enables direct evaluation of integrability and energy consistency.

In addition to technical challenges, a cultural gap exists between the applied mathematics and engineering communities regarding hypoelastic models. Much of the foundational work [24, 32] and the recent developments [39–41] regarding integrability and objectivity have been developed in mathematically rigorous frameworks. Consequently, these insights often remain inaccessible to practicing engineers and computational modelers. In contrast, computational investigations have primarily concentrated on developing accurate stress integration algorithms without necessarily adhering to the theoretical conditions for integrability [15, 26, 42, 43]. As a

result, important theoretical insights are not always translated into practical modeling guidelines.

This paper addresses these issues by presenting an open-source numerical framework designed to systematically evaluate the numerical integrability of hypoelastic formulations. Rather than offering a purely theoretical review of known limitations, we provide a computational diagnostic tool that bridges the gap between abstract mathematical conditions and finite element implementation.

The original contribution of this work is the development of a numerical platform capable of implementing and evaluating diverse hypoelastic formulations within a unified framework. Unlike traditional studies often limited to analytical material-point proofs, this platform enables a comprehensive numerical assessment of integrability across multiple mechanical problems – from single material points to complex boundary value problems. By leveraging the automatic differentiation and pseudo-symbolic capabilities of FEniCSx, we provide a tool for researchers to verify the numerical energetic consistency and path-independence of stress-rate models directly. We demonstrate the utility of this approach in Section 3.4 by implementing an Eulerian hyperelastic formulation, moving beyond standard 'grade-zero' hypoelasticity to show how the framework can validate highly non-linear, non-constant stiffness tensors.

To this end, we formulate hypoelasticity within a full Lagrangian framework, departing from the more common Eulerian or updated Lagrangian descriptions. This choice enhances control over kinematics, prevents geometric error accumulation, ensures consistent reference frames and reduces mesh sensitivity – particularly in problems involving large deformations and material nonlinearities. The approach is implemented in the open-source FEniCSx platform [44–47], by providing a pseudo-symbolic environment where automatic differentiation allows for direct control over objective rates and stiffness tensors. By moving beyond material-point analysis, our methodology build benchmark tests under cyclic and non-proportional loading to explicitly expose spurious energy accumulation. This establishes a reproducible basis for assessing the reliability of hypoelastic formulations in practical, large-deformation simulations.

The paper is structured as follows. Section 2 details the theoretical foundations and numerical procedures for implementing a consistent hypoelastic formulation within a finite element framework. Section 3 presents the benchmark problems and corresponding numerical results used to assess the proposed approach. By bridging theoretical and practical perspectives, we aim to support the development of physically consistent stress-rate formulations and enhance the reliability of nonlinear simulations involving hypoelastic formulations of materials response. This approach is illustrated in Section 3.4, which applies the numerical framework to test a non-constant stiffness model derived from Exponentiated Hencky energy. By moving beyond the standard grade-zero case, this section demonstrates the framework's capability to assess hypoelastic formulations featuring non-constant stiffness based on Eulerian strain energy.

2 Methods

Hypoelasticity is usually defined in a Eulerian framework, through the definition of the stress rate of the Cauchy or Kirchhoff stress tensor. Numerical methods for such constitutive model usually use updated Lagrangian formulation to solve the mechanical equilibrium. In our study, we use a Lagrangian formulation to simplify the numerical expenses linked to mesh evolution. In Sect. 2.1, we present the finite strain kinematic and the specific quantities used and defined in Eulerian hypoelasticity. In Sect. 2.2, we present the mechanical equilibrium, its formulation in a Lagrangian context and the proposed formulation of the explicit linearization of the equilibrium for a stress-rate formulation of the constitutive model. Sect. 2.3 presents the considered hypoelastic constitutive models. Sect. 2.5 presents the numerical implementation in the FeniCSx framework. Finally, Sect. 2.4 presents a new theoretical formulation for non-constant Eulerian stiffness derived from a Hencky-based strain energy. This approach is implemented and tested within the previously developed numerical framework to evaluate its behavior in a hypoelastic context.

2.1 Finite Strain Kinematics

Let consider a body $\mathcal{B}$ and its boundary $\partial\mathcal{B} = \partial\mathcal{B}_t \cup \partial\mathcal{B}_u$, where $\partial\mathcal{B}_t$ refers to the Neumann boundary condition and $\partial\mathcal{B}_u$ to the Dirichlet boundary condition. The body is defined by a position vector field $\mathbf{x}$ in the current configuration. It is mapped to the reference configuration $\mathcal{B}_0$, described by a field of position vector $\mathbf{X}$ through the transformation map $\boldsymbol{\varphi}$ defined as:

$$\mathbf{x} = \boldsymbol{\varphi}(\mathbf{X}, t) = \mathbf{X} + \mathbf{u}\,, \tag{1}$$

with $\mathbf{u}$ as the displacement field. With these considerations, we use the standard definitions of finite strain kinematics.

The deformation gradient [1] is,

$$\mathbf{F} = \frac{\partial \mathbf{x}}{\partial \mathbf{X}} = \mathbf{1} + \nabla_{\mathrm{X}}\mathbf{u}\,, \tag{2}$$

with $\mathbf{1}$ the second order identity tensor. The determinant of the transformation denote the change of volume during the transformation,

$$J = J(\mathbf{X}, t) = \det(\mathbf{F}(\mathbf{X}, t))\,. \tag{3}$$

The left Cauchy-Green strain tensor is a Eulerian strain measure used in defining the objective derivatives (see Sect. 2.3.1). It is defined as,

$$\mathbf{b} = \mathbf{F} \cdot \mathbf{F}^T\,, \tag{4}$$

with $\cdot$ the simple contraction operation and T the transpose operation. Its spectral decomposition reads,

[1] For any field $\mathbf{a}$, the gradients operators are defined in the reference and the current configuration respectively as: $\dfrac{\partial \mathbf{a}}{\partial \mathbf{X}} = \nabla_{\mathrm{X}}\mathbf{a}$ and $\dfrac{\partial \mathbf{a}}{\partial \mathbf{x}} = \nabla_{\mathrm{x}}\mathbf{a}$

$$\mathbf{b} = \sum_{\alpha} \chi_\alpha \mathbf{p}_\alpha \otimes \mathbf{p}_\alpha \,, \tag{5}$$

with χ_α and $\mathbf{p}_\alpha$ respectively the eigenvalues and eigenvectors of $\mathbf{b}$. In the Lagrangian formulation of the mechanical equilibrium, the strain measure used is the Green-Lagrange strain tensor, which reads,

$$\mathbf{E} = \frac{1}{2}\left(\mathbf{F}^T \cdot \mathbf{F} - \mathbf{1}\right) . \tag{6}$$

We also consider the left stretch tensor $\mathbf{V}$ and the rotation matrix $\mathbf{R}$ as the right polar decomposition of the deformation gradient:

$$\mathbf{F} = \mathbf{V} \cdot \mathbf{R} \,. \tag{7}$$

We define now a velocity field, $\mathbf{v}(\mathbf{X}, t)$ as:

$$\mathbf{v}(\mathbf{X}, t) = \dot{\mathbf{u}}(\mathbf{X}, t)^{[2]} \,, \tag{8}$$

for which it results:

$$\mathbf{v}(\mathbf{X}, t) = \frac{\partial \mathbf{u}}{\partial t}(\mathbf{X}, t) \,, \tag{9}$$

since $\mathbf{u}$ is a Lagrangian field. The strain rate is defined as the variation of the deformation gradient:

$$\dot{\mathbf{F}} = \nabla_{\mathbf{X}} \mathbf{v}(\mathbf{X}, t) \,. \tag{10}$$

The associated variation of the Green Lagrange tensor is:

$$\dot{\mathbf{E}} = \frac{1}{2}\left(\mathbf{F}^T \cdot \dot{\mathbf{F}} + \dot{\mathbf{F}}^T \cdot \mathbf{F}\right) . \tag{11}$$

In the deformed configuration, the spatial velocity gradient is defined as:

$$\mathbf{l}(\mathbf{x}, t) = \nabla_{\mathbf{x}} \mathbf{v}(\mathbf{x}, t) = \frac{\partial \mathbf{v}}{\partial \mathbf{x}}(\mathbf{x}, \mathbf{t}) = \frac{\partial \mathbf{v}}{\partial \mathbf{X}}(\mathbf{X}, \mathbf{t}) \cdot \frac{\partial \mathbf{X}}{\partial \mathbf{x}} \,. \tag{12}$$

Hence, the spatial velocity gradient is:

$$\mathbf{l} = \dot{\mathbf{F}} \cdot \mathbf{F}^{-1} \,. \tag{13}$$

The Eulerian strain rate and the spin tensor are defined respectively as the symmetric and skew-symmetric part of the spatial velocity gradient:

$$\mathbf{d} = \frac{1}{2}(\mathbf{l} + \mathbf{l}^T) \,, \tag{14}$$

$$\boldsymbol{\omega} = \frac{1}{2}(\mathbf{l} - \mathbf{l}^T) \,. \tag{15}$$

[2] The dot superscript denotes the material time derivative: $\dot{\mathbf{a}} = \frac{\mathrm{D}\mathbf{a}}{\mathrm{D}t}$

Finally, we define the Hencky strain $\boldsymbol{\eta}$, as a Eulerian measure of the strain. It is based on the polar decomposition of the deformation gradient $\mathbf{F} = \mathbf{VR}$ and reads:

$$\boldsymbol{\eta} = \ln \mathbf{V} = \frac{1}{2} \ln \mathbf{b} \tag{16}$$

In practice we compute it using the spectral decomposition of the left Cauchy-Green strain tensor in eq. (5). With χ_α and $\mathbf{p}_\alpha$ respectively the eigenvalues and eigenvectors of $\mathbf{b}$, the Hencky strain reads:

$$\boldsymbol{\eta} = \sum_\alpha \frac{1}{2} \ln \chi_\alpha \mathbf{p}_\alpha \otimes \mathbf{p}_\alpha \,. \tag{17}$$

2.2 Mechanical Equilibrium

We use the standard definitions of the stress tensors, with the notations introduced in Table 1.

Stress	$\boldsymbol{\sigma}$	$\boldsymbol{\tau}$	$\mathbf{P}$	$\mathbf{S}$
Cauchy $\boldsymbol{\sigma}$	$\boldsymbol{\sigma}$	$J^{-1}\boldsymbol{\tau}$	$J^{-1}\mathbf{P} \cdot \mathbf{F}^T$	$J^{-1}\mathbf{F} \cdot \mathbf{S} \cdot \mathbf{F}^T$
Kirchhoff $\boldsymbol{\tau}$	$J\boldsymbol{\sigma}$	$\boldsymbol{\tau}$	$\mathbf{P} \cdot \mathbf{F}^T$	$\mathbf{F} \cdot \mathbf{S} \cdot \mathbf{F}^T$
1st Piola-Kirchhoff $\mathbf{P}$	$J\boldsymbol{\sigma} \cdot \mathbf{F}^{-T}$	$\boldsymbol{\tau} \cdot \mathbf{F}^{-T}$	$\mathbf{P}$	$\mathbf{F} \cdot \mathbf{S}$
2nd Piola-Kirchhoff $\mathbf{S}$	$J\mathbf{F}^{-1} \cdot \boldsymbol{\sigma} \cdot \mathbf{F}^{-T}$	$\mathbf{F}^{-1} \cdot \boldsymbol{\tau} \cdot \mathbf{F}^{-T}$	$\mathbf{F}^{-1} \cdot \mathbf{P}$	$\mathbf{S}$

Table 1: Stress tensors and their *pull-back/push-forward* operations. Table inspired from Nemat-Nasser [14]

We consider a quasi-static formulation without initial pre-stress and volumetric forces. The local form of the balance of linear momentum reads in the current configuration:

$$\begin{cases} \nabla_{\mathrm{x}} \cdot \boldsymbol{\sigma} = 0 & \text{in } \mathcal{B}\,, \\ \mathbf{u} = \mathbf{u}_d & \text{on } \partial\mathcal{B}_u\,, \\ \boldsymbol{\sigma} \cdot \mathbf{n} = \mathbf{t}_d & \text{on } \partial\mathcal{B}_t\,. \end{cases} \tag{18}$$

whereby $\nabla_{\mathrm{x}}\cdot$ is the divergence operator, $\mathbf{n}$ is the outer normal unit vector, $\mathbf{u}_d$ and $\mathbf{t}_d$ are the imposed displacement field and surface traction field.

In a Lagrangian formulation, the equilibrium is *pulled-back* in the reference configuration, with the 1st Piola-Kirchhoff stress tensor:

$$\begin{cases} \nabla_{\mathrm{X}} \cdot \mathbf{P} = 0 & \text{in } \mathcal{B}_0\,, \\ \mathbf{u} = \mathbf{u}_d & \text{on } \partial\mathcal{B}_{u0}\,, \\ \mathbf{P} \cdot \mathbf{N} = \mathbf{t}_{d0} = J\boldsymbol{\sigma} \cdot \mathbf{F}^{-T} \cdot \mathbf{N} & \text{on } \partial\mathcal{B}_{t0}\,. \end{cases} \tag{19}$$

2.2.1 Weak form

The numerical (Finite-Element) solution of the balance of linear momentum is obtained from the weak form of the partial differential problem defined in Eq. (18) or (19). In this Lagrangian formulation, Eq. (19) is considered. For $\mathbf{u}_{sol}$ the displacement field, solution of the equilibrium, the weak form reads, for every virtual field $\boldsymbol{v}^*$ admissible with the boundary conditions:

$$G(\mathbf{u}_{sol}, \boldsymbol{v}^*) = \int_{\mathcal{B}_0} \mathbf{P}(\mathbf{u}_{sol}) : \nabla_{\mathbf{X}} \boldsymbol{v}^* dV - \int_{\partial \mathcal{B}_{t0}} \mathbf{t}_{d0} \cdot \boldsymbol{v}^* dA = 0 \qquad , \forall \boldsymbol{v}^* \,. \tag{20}$$

Using the symmetric second Piola-Kirchhoff tensor $\mathbf{S} = \mathbf{F}_{sol}^{-1} \cdot \mathbf{P}$ and the virtual Green-Lagrange tensor $\delta\mathbf{E}(\mathbf{u}_{sol}, \boldsymbol{v}^*) = \frac{1}{2}\left(\mathbf{F}_{sol}^T \cdot \nabla_{\mathbf{X}} \boldsymbol{v}^* + \nabla_{\mathbf{X}} \boldsymbol{v}^{*T} \cdot \mathbf{F}_{sol}\right)$, the weak form can be rewritten as:

$$G(\mathbf{u}_{sol}, \boldsymbol{v}^*) = \int_{\mathcal{B}_0} \mathbf{S}(\mathbf{u}_{sol}) : \delta\mathbf{E}(\mathbf{u}_{sol}, \boldsymbol{v}^*) dV - \int_{\partial \mathcal{B}_{t0}} \mathbf{t}_{d0} \cdot \boldsymbol{v}^* dA = 0 \qquad , \forall \boldsymbol{v}^* \,. \tag{21}$$

Since this is a non-linear problem, the solution $\mathbf{u}_{sol}$ is obtained by minimizing the residuals using a Newton-Raphson procedure (see Section 2.5.1). To apply this iterative method, the weak form of the equilibrium equations must be linearized, as the Newton-Raphson algorithm requires a linearized formulation to compute updates to the solution at each iteration.

2.2.2 Linearization

Let us consider an unknown displacement field $\overline{\mathbf{u}}$, close to the exact solution $\mathbf{u}_{sol}$. Around this configuration, the residuals are linearized by considering the directional derivative of the weak form $G(\mathbf{u}, \boldsymbol{v}^*)$ computed at $\mathbf{u} = \overline{\mathbf{u}}$, alongside the displacement direction $\Delta\mathbf{u}$, that is $\mathrm{D}G(\overline{\mathbf{u}}, \boldsymbol{v}^*) \cdot \Delta\mathbf{u}$. Then,

$$L[G]_{\mathbf{u}=\overline{\mathbf{u}}} = G(\overline{\mathbf{u}}, \boldsymbol{v}^*) + \mathrm{D}G(\overline{\mathbf{u}}, \boldsymbol{v}^*) \cdot \Delta\mathbf{u}, \tag{22}$$

Where, the directional derivative of the functional $G(\overline{\mathbf{u}}, \boldsymbol{v}^*)$ is defined as:

$$\mathrm{D}G(\overline{\mathbf{u}}, \boldsymbol{v}^*) = \lim_{\alpha \to 0} \frac{G(\overline{\mathbf{u}} + \alpha\Delta\mathbf{u}, \boldsymbol{v}^*) - G(\overline{\mathbf{u}}, \boldsymbol{v}^*)}{\alpha} = \left.\frac{\mathrm{d}G(\overline{\mathbf{u}} + \alpha\Delta\mathbf{u}, \boldsymbol{v}^*)}{\mathrm{d}\alpha}\right|_{\alpha=0} \tag{23}$$

In this section, for any field $\mathbf{a}$, the symbol $\overline{\mathbf{a}}$ denotes the value of $\mathbf{a}$ in the configuration reached by the displacement $\mathbf{u} = \overline{\mathbf{u}}$. Accordingly, the virtual incremental Green–Lagrange strain tensor is expressed as:

$$\delta\overline{\mathbf{E}} = \frac{1}{2}(\overline{\mathbf{F}}^T \cdot \nabla_{\mathrm{X}} \boldsymbol{v}^* + \nabla_{\mathrm{X}} \boldsymbol{v}^{*T} \cdot \overline{\mathbf{F}}) \,. \tag{24}$$

Since $\overline{\mathbf{u}}$ is not the solution, the residuals R are not null and read:

$$R = G(\overline{\mathbf{u}}, \boldsymbol{v}^*) = \int_{\mathcal{B}} \overline{\mathbf{S}} : \delta\overline{\mathbf{E}} dV - \int_{\partial\mathcal{B}_{t0}} \mathbf{T}_d \cdot \boldsymbol{v}^* dA \qquad , \forall \boldsymbol{v}^* \,. \tag{25}$$

The directional derivative of the residuals is:

$$\mathrm{D}G(\overline{\mathbf{u}}, \boldsymbol{v}^*) \cdot \Delta\mathbf{u} = \int_{\mathcal{B}} \left[\nabla_{\mathrm{X}} \Delta\mathbf{u} \cdot \overline{\mathbf{S}} : \nabla_{\mathrm{X}} \boldsymbol{v}^* + \delta\overline{\mathbf{E}} : \mathrm{D}\mathbf{S}(\overline{\mathbf{u}}) \cdot \Delta\mathbf{u} \right] dV \,, \tag{26}$$

where $\mathrm{D}\mathbf{S}(\overline{\mathbf{u}}) \cdot \Delta\mathbf{u}$ is the directional derivative of the stress tensor, which is defined by the hypoelastic constitutive law. Indeed with an abuse of notation, the directional derivative and the stress rate of the Second Piola-Kirchhoff stress tensor are associated and read:

$$\mathrm{D}\mathbf{S}(\overline{\mathbf{u}}) \cdot \Delta\mathbf{u} = \dot{\mathbf{S}} \Delta t \,, \tag{27}$$

with Δt the increment of time corresponding to the increment of displacement $\Delta\mathbf{u}$ for a velocity field $\dot{\mathbf{u}}$.

2.3 Grade-zero hypoelastic constitutive modelling

This section presents the constitutive relationship for grade-zero hypoelasticity. As defined by Truesdell [48], a hypoelastic material is a material whose constitutive behavior is defined by a stress rate. Such stress rate depends on the stress state and on the strain rate, however the resulting stress state has to be independent from the strain rate. Let us consider a measure of the stress $\boldsymbol{s}$, a measure of the strain rate $\boldsymbol{d}$ and an objective measure of the stress rate $\mathring{\boldsymbol{s}}$. The constitutive behavior of a hypoelastic model is defined as:

$$\mathring{\boldsymbol{s}} = \mathcal{G}(\boldsymbol{s}, \boldsymbol{d}) \,, \tag{28}$$

where $\mathcal{G}$ is a given function. To guarantee frame indifference, an objective derivative must be employed in the hypoelastic constitutive relation given in Eq. (28) [15, 21]. In grade-zero hypoelasticity, an arbitrary objective derivative $\mathring{\boldsymbol{\tau}}$ of the Kirchhoff stress $\boldsymbol{\tau}$ is defined as directly proportional to the strain rate $\mathbf{d}$, through a constant Eulerian stiffness tensor $\mathbb{c}$.

$$\mathring{\boldsymbol{\tau}} = \mathbb{c} : \mathbf{d} \,. \tag{29}$$

For isotropic constitutive responses, $\mathbb{c}$ is expressed through the Lamé coefficients, λ and μ, as:

$$\mathbb{c} = 2\mu\mathbb{I} + \lambda \mathbf{1} \otimes \mathbf{1} \,, \tag{30}$$

with $\mathbb{I}$ as the fourth-order identity tensor. Hence, it results in:

$$\mathring{\boldsymbol{\tau}} = \mathbb{c} : \mathbf{d} = 2\mu\mathbf{d} + \lambda(\mathrm{Tr}\,\mathbf{d})\mathbf{1} \,. \tag{31}$$

2.3.1 Hypoelastic laws with different objective derivatives

In this section, we present the various objective stress rate formulations considered in the numerical benchmark cases. Specifically, we examine the Oldroyd, Jaumann, Green–Naghdi and logarithmic stress rate definitions. The hypoelastic constitutive law based on the Oldroyd objective derivative can be expressed as:

$$\mathring{\boldsymbol{\tau}}^{o} = \mathcal{L}_v[\boldsymbol{\tau}] = \dot{\boldsymbol{\tau}} - \boldsymbol{\tau}\cdot\mathbf{l}^T - \mathbf{l}\cdot\boldsymbol{\tau} = \mathbb{c} : \mathbf{d}\,, \tag{32}$$

where we highlight that the Oldroyd derivative of the Kirchhoff stress is equivalent to the Lie derivative [21]. By using the Zaremba-Jaumann derivative, one of the most commonly used objective derivative, we get:

$$\mathring{\boldsymbol{\tau}}^{j} = \dot{\boldsymbol{\tau}} + \boldsymbol{\tau}\cdot\boldsymbol{\omega} - \boldsymbol{\omega}\cdot\boldsymbol{\tau} = \mathbb{c} : \mathbf{d}\,. \tag{33}$$

Another commonly used objective derivative is the Green-Naghdi derivative. It is defined based on the rigid spin tensor $\boldsymbol{\Omega} = \dot{\mathbf{R}}\cdot\mathbf{R}^T$, where $\mathbf{R}$ is the rotation matrix defined through the polar decomposition of the deformation gradient (see Eq. (7)). This objective derivative leads to the hypoelastic law:

$$\mathring{\boldsymbol{\tau}}^{\mathrm{GN}} = \dot{\boldsymbol{\tau}} + \boldsymbol{\tau}\cdot\boldsymbol{\Omega} - \boldsymbol{\Omega}\cdot\boldsymbol{\tau} = \mathbb{c} : \mathbf{d}\,. \tag{34}$$

In practice, the rigid spin tensor is used through its decomposition, see [49]:

$$\boldsymbol{\Omega} = \boldsymbol{\omega} + \boldsymbol{\Upsilon}^{GN} = \boldsymbol{\omega} + \sum_{\alpha\neq\beta}\left(\frac{\sqrt{\chi_\beta}-\sqrt{\chi_\alpha}}{\sqrt{\chi_\beta}+\sqrt{\chi_\alpha}}\right)(\mathbf{p}_\alpha\otimes\mathbf{p}_\alpha)\cdot\mathbf{d}\cdot(\mathbf{p}_\beta\otimes\mathbf{p}_\beta)\,. \tag{35}$$

where χ_α and $\mathbf{p}_\alpha$ are the eigenvalues and eigenvectors of the left Cauchy-Green strain tensor $\mathbf{b}$, obtained from its spectral decomposition (see Eq. (5)).

Through their extensive work, Xiao et al. [27, 30, 31, 32, 49, 50, 51] showed that the objective derivatives defined in Eqs. (32) to (34) are not integrable for grade-zero hypoelasticity [27]. They developed the logarithmic objective stress rate and proved that this is the only framework that is integrable for a grade-zero hypoelastic material [21, 27, 32].

The hypoelastic law defined from the logarithmic derivative leads to:

$$\mathring{\boldsymbol{\tau}}^{log} = \dot{\boldsymbol{\tau}} + \boldsymbol{\tau}\cdot\boldsymbol{\Omega}^{log} - \boldsymbol{\Omega}^{log}\cdot\boldsymbol{\tau} = \mathbb{c} : \mathbf{d}\,, \tag{36}$$

$$\boldsymbol{\Omega}^{log} = \boldsymbol{\omega} + \boldsymbol{\Upsilon}^{log} = \boldsymbol{\omega} + \sum_{\alpha\neq\beta}\left(\frac{\chi_\alpha+\chi_\beta}{\chi_\beta-\chi_\alpha} + \frac{2}{\ln(\chi_\alpha/\chi_\beta)}\right)(\mathbf{p}_\alpha\otimes\mathbf{p}_\alpha)\cdot\mathbf{d}\cdot(\mathbf{p}_\beta\otimes\mathbf{p}_\beta)\,. \tag{37}$$

In Eqs. (35) and (37), the relative spin tensors $\boldsymbol{\Upsilon}^{GN}$ and $\boldsymbol{\Upsilon}^{log}$ describe the difference between the Eulerian spin tensor $\boldsymbol{\omega}$ and the rigid spin $\boldsymbol{\Omega}$ or the logarithmic spin tensor $\boldsymbol{\Omega}^{log}$, respectively. This decomposition serves to simplify the notation when considering the Lie-derivative proxy for the pull-back operation in Eqs. (43) and (44), providing a unified algebraic structure for the different objective rates investigated in this work.

2.3.2 Stress rates: from Eulerian to Lagrangian formulation

When solving the mechanical equilibrium in the Lagrangian formulation, we need to pull back the constitutive law from the Eulerian current configuration to the Lagrangian reference configuration. The stress rate $\dot{\mathbf{S}}$ required in Eqs. (26) and (27) is obtained from the pull-back operation on the Lie derivative of the Kirchhoff stress tensor.

$$\dot{\mathbf{S}} = \mathbf{F}^{-1} \cdot \mathcal{L}_v[\boldsymbol{\tau}] \cdot \mathbf{F}^{-T} \,. \tag{38}$$

Starting from different objective stress rates, the corresponding expression of the Lie derivative changes. The Oldroyd rate is naturally:

$$\mathcal{L}_v[\boldsymbol{\tau}] = \mathring{\boldsymbol{\tau}}^o = \mathbb{c} : \mathbf{d} \,. \tag{39}$$

More generally, the Lie derivative can be expressed through the material time derivative:

$$\mathcal{L}_v[\boldsymbol{\tau}] = \dot{\boldsymbol{\tau}} - \boldsymbol{\tau} \cdot \mathbf{l}^T - \mathbf{l} \cdot \boldsymbol{\tau} \,. \tag{40}$$

Starting from Eq. (33), we get:

$$\dot{\boldsymbol{\tau}} = \mathring{\boldsymbol{\tau}}^j - \boldsymbol{\tau} \cdot \boldsymbol{\omega} + \boldsymbol{\omega} \cdot \boldsymbol{\tau} \,. \tag{41}$$

and since $\mathbf{l} = \mathbf{d} + \boldsymbol{\omega}$ and $\boldsymbol{\omega}^T = -\boldsymbol{\omega}$, the Lie derivative obtained from Eq. (40) and a hypoelastic law based on the Jauman rate (Eq. (33)) reads:

$$\mathcal{L}_v[\boldsymbol{\tau}] = \mathring{\boldsymbol{\tau}}^j - \boldsymbol{\tau} \cdot \mathbf{d} - \mathbf{d} \cdot \boldsymbol{\tau} = \mathbb{c} : \mathbf{d} - \boldsymbol{\tau} \cdot \mathbf{d} - \mathbf{d} \cdot \boldsymbol{\tau} \,. \tag{42}$$

The same procedure, starting from a hypoelastic law based on the Green-Naghdi rate (Eq. (34)), leads to:

$$\mathcal{L}_v[\boldsymbol{\tau}] = \mathbb{c} : \mathbf{d} - \boldsymbol{\tau} \cdot (\mathbf{d} + \boldsymbol{\Upsilon}^{GN}) + (\boldsymbol{\Upsilon}^{GN} - \mathbf{d}) \cdot \boldsymbol{\tau} \,. \tag{43}$$

where the decomposition $\boldsymbol{\Omega} = \boldsymbol{\omega} + \boldsymbol{\Upsilon}^{GN}$ has been exploited. A hypoelastic laws based on the logarithmic rate (Eqs. (36) and (37)) leads to the definition of the Lie derivative as:

$$\mathcal{L}_v[\boldsymbol{\tau}] = \mathbb{c} : \mathbf{d} - \boldsymbol{\tau} \cdot (\mathbf{d} + \boldsymbol{\Upsilon}^{log}) + (\boldsymbol{\Upsilon}^{log} - \mathbf{d}) \cdot \boldsymbol{\tau} \,. \tag{44}$$

where the decomposition $\boldsymbol{\Omega}^{log} = \boldsymbol{\omega} + \boldsymbol{\Upsilon}^{log}$ has been exploited.

2.4 Beyond grade-zero hypoelasticity

In practice, hypoelastic constitutive models implemented in finite element frameworks are largely limited to grade-zero formulations, characterized by a constant Eulerian stiffness tensor. As emphasized by Lin [21], an arbitrary choice of an evolving stiffness tensor, i.e one depending on strain measures without satisfying appropriate consistency conditions, generally leads to non-integrable constitutive behavior. This path-dependence constitutes a major theoretical limitation, as grade-zero models are

unable to reproduce the complex nonlinear responses observed at finite strains. Consequently, there is a strong motivation to formulate nonlinear hypoelastic models within a more rigorous theoretical setting. Identifying a consistent framework for defining an evolving stiffness tensor is essential to extend finite-strain modeling capabilities, especially for viscoplastic and hypoplastic formulations that are naturally expressed in terms of Eulerian stress rates.

The inherent limitation of grade-zero formulations is illustrated in Fig. 1. Under uniaxial loading, the constant Eulerian stiffness of the grade-zero model results in a response that fails to capture the progressive stiffening characteristic of many engineering and biological materials. By contrast, the exponentiated Hencky energy introduced by Neff et al. [52] serves as the basis for our evolving stiffness tensor. This formulation introduces controlled nonlinearity through the parameters k and $\hat{k}$ (cf., the following Eq. (52)), allowing for the reproduction of the "J-shaped" stress-strain curves typical of biological tissue stiffening [53, 54].

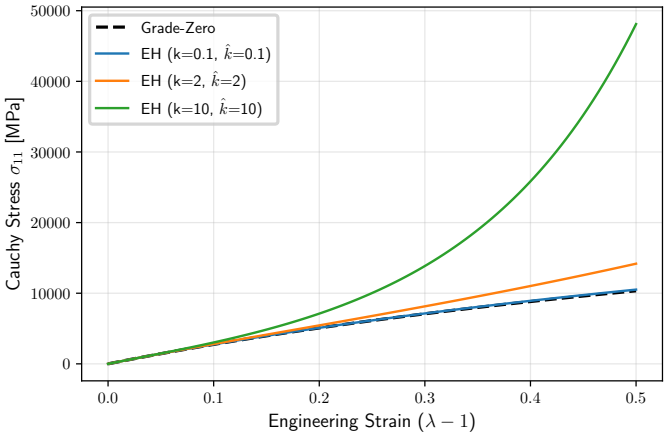

Fig. 1: Uniaxial strain-stress relationship comparison. The grade-zero (GZ) model exhibits a linear-like response in Hencky space, failing to reproduce material stiffening. The Exponentiated-Hencky (EH) model, driven by parameters $(k, \hat{k})$ (see Eq. (52)), captures the highly non-linear J-shaped curve observed in biological tissues and soft polymers.

In this work, we investigate from a numerical standpoint the feasibility of constructing a non-constant stiffness tensor that yields an integrable hypoelastic formulation. Our approach is motivated by the foundational result of Noll [18], who demonstrated that any hyperelastic model admits an equivalent hypoelastic representation in terms of stress rates (see Eq. (28)). Building on this result, Eshraghi et al. [8] proposed a Eulerian integrable hypoelastic model obtained by applying a push-forward operation to a stiffness tensor defined in the Lagrangian configuration from a hyperelastic strain-energy density. More recently, Neff et al. [52] showed that the exponentiated Hencky

energy provides a consistent framework for Eulerian hyperelasticity, based on a strain-energy density expressed in terms of the Hencky strain, a Eulerian strain measure. Motivated by these developments, we explore the use of Eulerian hyperelastic constitutive relations as a basis for defining a non-constant stiffness tensor directly in the current configuration.

Following Neff et al. [52], we consider a strain-energy density function expressed in terms of the Hencky strain $\boldsymbol{\eta} = \ln \mathbf{V}$, as defined in Eq. 16:

$$\mathfrak{w}_{int} : \boldsymbol{\eta} \mapsto \mathfrak{w}_{int}(\boldsymbol{\eta}) \,. \tag{45}$$

Within the logarithmic corotational framework, a direct kinematic relationship exists between the Hencky strain and the Eulerian rate of deformation tensor $\mathbf{d}$. As shown by Xiao et al. [30], Xiao [55], the logarithmic objective rate of the Hencky strain coincides exactly with the strain rate, yielding:

$$\mathbf{d} = \mathring{\boldsymbol{\eta}}^{log} = \dot{\boldsymbol{\eta}} + \boldsymbol{\eta} \cdot \boldsymbol{\Omega}^{log} - \boldsymbol{\Omega}^{log} \cdot \boldsymbol{\eta} \,. \tag{46}$$

We then follow the classical hyperelastic procedure for deriving stresses and corresponding stress rates [56], here adapted to a Eulerian setting by employing the appropriate corotational derivative of the elastic potential. Taking the logarithmic objective derivative of the internal energy leads to the definition of the internal power p_{int}. By performing a change of variable and exploiting the kinematic identity provided by the logarithmic rate of the Hencky strain, one recovers the standard expression linking internal power to the work conjugacy between the Kirchhoff stress and the strain rate [57].

$$p_{int} = \mathring{\mathfrak{w}}_{int}^{log} = \frac{\partial \mathfrak{w}_{int}}{\partial \boldsymbol{\eta}} : \mathring{\boldsymbol{\eta}}^{log} = \boldsymbol{\tau} : \mathbf{d} \,. \tag{47}$$

The Kirchhoff stress tensor is thus derived from the strain energy density function [58] as:

$$\boldsymbol{\tau} = \frac{\partial \mathfrak{w}_{int}}{\partial \boldsymbol{\eta}} \,. \tag{48}$$

The logarithmic objective derivative on the stress tensor yields:

$$\mathring{\boldsymbol{\tau}}^{log} = \frac{\partial^2 \mathfrak{w}_{int}}{\partial \boldsymbol{\eta} \partial \boldsymbol{\eta}} : \mathbf{d} \,. \tag{49}$$

The Eulerian stiffness tensor $\mathbb{c}$ is defined through the consistent application of the logarithmic objective derivative to the stress tensor. The inconsistent use of an objective stress rate other than the logarithmic rate – such as those based on the Jaumann or Green–Naghdi rates – in conjunction with the strain rate $\mathbf{d}$ is a source of non-integrability. This observation does not imply that these objective stress rates are intrinsically non-integrable; rather, integrability requires that each stress rate be paired with its energetically conjugate strain rate, which must be derived from the corresponding objective rate applied to the appropriate Eulerian strain measure.

Hence, the Eulerian stiffness tensor is obtained as the second derivative of a Eulerian hyperelastic potential with respect to its state variable, namely the Hencky strain measure, yielding:

$$\mathring{\boldsymbol{\tau}}^{log} = \mathbb{c} : \mathbf{d} \Rightarrow \mathbb{c}(\boldsymbol{\eta}) = \frac{\partial^2 w_{int}}{\partial \boldsymbol{\eta} \partial \boldsymbol{\eta}} \,. \tag{50}$$

We explore whether this formulation can yield an integrable stress-rate model within an Eulerian configuration. While a formal proof of integrability is not provided, in the forthcoming case studies, we will numerically assess the model's performance by monitoring spurious energy generation. By exploiting the automatic differentiation capabilities of FEniCSx, we consistently and straightforwardly obtain the Eulerian stiffness tensor and integrate it via the logarithmic objective derivative (Eq. (44)). This numerical framework is evaluated by comparing two strain-energy density functions: grade-zero energy and exponentiated Hencky energy.

2.4.1 Grade-Zero energy

In the Lagrangian configuration, the Saint-Venant energy density leads to a constant stiffness matrix. Hence, by drawing the direct parallel with the Hencky strain in the Eulerian configuration, we build the grade-zero energy, that is the eulerian strain energy density function that leads to a Eulerian constant stiffness matrix, i.e the grade-zero hypoelasticity [34]. It reads:

$$w_{GZ}(\boldsymbol{\eta}) = \frac{\lambda}{2}(\mathrm{Tr}(\boldsymbol{\eta}))^2 + \mu \mathrm{Tr}(\boldsymbol{\eta}^2) \,, \tag{51}$$

with λ and μ the classical Lame parameters. In this case, the Eulerian stiffness matrix remains the constant tensor defined in Eq. (30), recovering the classical grade-zero behavior.

2.4.2 Exponentiated Hencky Energy

We consider another eulerian energy density function. The exponentiated Hencky energy, introduced by [52], provides an isotropic highly non-linear law, leading to a non-constant stiffness matrix. Based on the Hencky strain, it introduces two additional parameters k and $\hat{k}$ that govern the degree of non-linearity relative to the grade-zero case:

$$w_{EH}(\boldsymbol{\eta}) = \frac{\lambda}{2\hat{k}} \left[\exp\left(\hat{k} (\mathrm{Tr}(\boldsymbol{\eta}))^2 \right) - 1 \right] + \frac{\mu}{k} \left[\exp\left(k \mathrm{Tr}(\boldsymbol{\eta}^2) \right) - 1 \right] \,. \tag{52}$$

This strain energy is consistent with the grade-zero energy in the limit:

$$w_{EH}(\boldsymbol{\eta}) \xrightarrow[(k,\hat{k}) \to (0,0)]{} w_{GZ}(\boldsymbol{\eta}) \,. \tag{53}$$

2.5 Numerical Implementation

The mechanical problem is solved by implementing three-dimensional hexahedron elements in the FeniCSx library in Python. This library uses domain-specific languages specifically designed for writing variational formulations of the balance laws. However, the mechanical problem is not explicitly defined in a variational formulation as a function of the displacement when we are using a hypoelastic formulation. Sections

2.5.1 and 2.5.2 present the adopted strategy used in the numerical implementation for a stress rate formulation of the constitutive model, and Section 2.5.3 briefly outlines the structure of the publicly-available code.

Eq. (21) presents the weak form of the mechanical equilibrium in a Lagrangian formulation. Its linearization around a given configuration is presented in Eq. (26). The hypoelastic formulation defines the stress rate in such given configuration, i.e the directional derivative of the stress as a function of the increment of displacement. In FeniCSx, the pseudo symbolic tools allow us to focus on the formulation of the PDEs and the directional derivatives are computed in an automatic way by the solver.

In the finite element model, the displacement field is discretized using Lagrange elements with continuous piecewise linear shape functions $\phi_i(\mathbf{X})$.

$$\mathbf{u} \in V \Leftrightarrow \mathbf{u}(\mathbf{X}) = \sum_{i=1}^{N} u_i \phi_i(\mathbf{X}) \,, \tag{54}$$

where u_i are the nodal values of the displacement field.

2.5.1 Solving the equilibrium

The linearized formulation of the weak form (Eqs. (25) and (26)) introduces explicitly the stress-rate constitutive models within the linearization of the residuals. The mechanical equilibrium can be solved by minimizing the residual with a standard Newton-Raphson procedure.

With a slight abuse of notation, let $\mathbf{u}_k$ be the vector collecting nodal displacement values associated with the configuration at the k-th iteration of the Newton-Raphson procedure. The second Piola-Kirchhoff stress tensor $\mathbf{S}_k$ is the stress tensor field corresponding to the configuration at the k-th iteration and it is computed from the last iteration, see Sect. 2.5.2. The residuals R_k are defined by:

$$R_k = G(\mathbf{u}_k, \boldsymbol{v}^*) = \int_{\mathcal{B}_0} \mathbf{S}_k : \delta\mathbf{E}_k dV - \int_{\partial\mathcal{B}_{t0}} \mathbf{t}_{d0} \cdot \boldsymbol{v}^* dA \,, \tag{55}$$

The Newton-Raphson process searches $\Delta\mathbf{u}_k$ that minimizes the linearized weak form. From Eq. (22), we get:

$$L[G]_{\mathbf{u}=\mathbf{u}_k} = G(\mathbf{u}_k, \boldsymbol{v}^*) + \mathrm{D}G(\mathbf{u}_k, \boldsymbol{v}^*) \cdot \Delta\mathbf{u}_k = 0 \,. \tag{56}$$

The linearization of the residuals presented in equation (26) gives the formulation of the tangent to the residuals.

$$\mathrm{D}G(\mathbf{u}_k, \boldsymbol{v}^*) \cdot \Delta\mathbf{u} = \int_{\mathcal{B}_0} \left[\nabla_{\mathrm{X}} \Delta\mathbf{u} \cdot \mathbf{S}_k : \nabla_{\mathrm{X}} \boldsymbol{v}^* + \delta\mathbf{E}_k : \mathrm{D}\mathbf{S}(\mathbf{u}_k) \cdot \Delta\mathbf{u}\right] dV \,, \tag{57}$$

with the directional derivative of the stress $\mathrm{D}\mathbf{S}(\mathbf{u}_k) \cdot \Delta\mathbf{u}$ defined from the pull back operation of the Lie derivative of the Kirchhoff stress tensor (cf. Eq. (38)):

$$\mathrm{D}\mathbf{S}(\mathbf{u}_k) \cdot \Delta\mathbf{u} = \mathbf{F}_k^{-1} \cdot \mathcal{L}_v[\boldsymbol{\tau}]_k(\Delta\mathbf{u}) \cdot \mathbf{F}_k^{-T} \,. \tag{58}$$

In what follows, we define $\mathbf{d}_k(\Delta\mathbf{u})$ as the incremental strain rate. It is the symmetric part of the incremental velocity gradient, which reads:

$$\mathbf{l}_k(\Delta\mathbf{u}) = \nabla_{\mathbf{X}}\Delta\mathbf{u}\cdot\mathbf{F}_k^{-1}\,. \tag{59}$$

For the Oldroyd derivative, the Lie derivative reads:

$$\mathcal{L}_v[\boldsymbol{\tau}]_k(\Delta\mathbf{u}) = \mathbb{c} : \mathbf{d}_k(\Delta\mathbf{u})\,. \tag{60}$$

For the Jaumann derivative, the Lie derivative reads:

$$\mathcal{L}_v[\boldsymbol{\tau}]_k(\Delta\mathbf{u}) = \mathbb{c} : \mathbf{d}_k(\Delta\mathbf{u}) - \boldsymbol{\tau}_k\cdot\mathbf{d}_k(\Delta\mathbf{u}) - \mathbf{d}_k(\Delta\mathbf{u})\cdot\boldsymbol{\tau}_k\,. \tag{61}$$

For the Green-Naghdi derivative, the Lie derivative reads:

$$\begin{aligned}\mathcal{L}_v[\boldsymbol{\tau}]_k(\Delta\mathbf{u}) = \mathbb{c} : \mathbf{d}_k(\Delta\mathbf{u}) - \boldsymbol{\tau}_k\cdot(\mathbf{d}_k(\Delta\mathbf{u}) + \boldsymbol{\Upsilon}_k^{GN}(\Delta\mathbf{u}))\\ + (\boldsymbol{\Upsilon}_k^{GN}(\Delta\mathbf{u}) - \mathbf{d}_k(\Delta\mathbf{u}))\cdot\boldsymbol{\tau}_k\,.\end{aligned} \tag{62}$$

For the logarithmic derivative, the Lie derivative reads:

$$\begin{aligned}\mathcal{L}_v[\boldsymbol{\tau}]_k(\Delta\mathbf{u}) = \mathbb{c} : \mathbf{d}_k(\Delta\mathbf{u}) - \boldsymbol{\tau}_k\cdot(\mathbf{d}_k(\Delta\mathbf{u}) + \boldsymbol{\Upsilon}_k^{log}(\Delta\mathbf{u}))\\ + (\boldsymbol{\Upsilon}_k^{log}(\Delta\mathbf{u}) - \mathbf{d}_k(\Delta\mathbf{u}))\cdot\boldsymbol{\tau}_k\,.\end{aligned} \tag{63}$$

Finally, the Newton-Raphson scheme (Eq. (56)) is broke down to a linear process, where the tangent matrix $\mathrm{D}G(\mathbf{u}_k, \boldsymbol{v}^*)$ and residual vector $G(\mathbf{u}_k, \boldsymbol{v}^*)$ are linked through:

$$\mathrm{D}G(\mathbf{u}_k, \boldsymbol{v}^*)\cdot\Delta\mathbf{u}_k = -G(\mathbf{u}_k, \boldsymbol{v}^*) \qquad ,\forall\boldsymbol{v}^*\,. \tag{64}$$

Numerically the tangent matrix $\mathrm{D}G(\mathbf{u}_k, \boldsymbol{v}^*)$ is obtained using the automatic differentiation tools of FeniCSx. The displacement vector $\Delta\mathbf{u}_k$ is obtained by solving Eq. (64). Once the displacement is known, the stress tensor is updated to compute the stress value required in the next step of the Newton-Raphson procedure (Eq. (57)). This update is carried out through the integration of the stress rate constitutive law, presented in next Sect. 2.5.2. The residuals are then computed for the $k+1$ iteration and the process continues until convergence is reached, that is until residuals are minimized $R_k < \epsilon$.

2.5.2 Integrating the stress increment

Once the displacement increment is obtained, the corresponding stress state $\mathbf{S}_{k+1}$ must be evaluated by integrating the stress rate along the displacement path. The common implementation of hypoelastic models is based on a Eulerian approach. As such it relies on algorithms that account for the evolution of the configuration during the displacement path. Specific algorithms have been developed for the different objective derivatives [21] and in various hypoelastic and hypoplastic conditions [34, 35, 59, 60].

Here, we adopt a Lagrangian perspective and focus on the integration of the second Piola–Kirchhoff stress tensor. The stress increment is defined as the path integral of the directional derivative of the stress with respect to the displacement. To avoid confusion between the real physical time and the artificial pseudo-time introduced by the Newton–Raphson iteration, we denote by s a curve parameter describing the displacement trajectory. In the discrete numerical context, following standard incremental

procedures for path-dependent problems [42, 61], this trajectory is parameterized by $s \in [0,1]$ and is written as:

$$\mathbf{u}(s) = \mathbf{u}_k + s\Delta\mathbf{u}_k \quad , \quad s \in [0,1]\,, \tag{65}$$

where, $\mathbf{u}(s=0) = \mathbf{u}_k$ and $\mathbf{u}(s=1) = \mathbf{u}_{k+1}$. The stress evolution along this path is then expressed as:

$$\mathbf{S}(\mathbf{u}) = \mathbf{S}(\mathbf{u}_k) + \int_0^s \mathrm{D}\mathbf{S}(\mathbf{u}_k + s^*\Delta\mathbf{u}_k)\cdot\Delta\mathbf{u}_k\, ds^*\,, \tag{66}$$

where the directional derivative of the stress is defined according to Eqs. (58)–(63) for an infinitesimal displacement increment $\Delta\mathbf{u}_k\, ds^*$. Accordingly, the stress integration procedure for the Newton–Raphson step from iteration k to iteration $k+1$ is formally written as:

$$\begin{cases} \mathbf{u}_{k+1} = \mathbf{u}_k + \Delta\mathbf{u}_k\,, \\ \mathbf{S}_{k+1} = \mathbf{S}_k + \displaystyle\int_{s^*=0}^{1} \mathrm{D}\mathbf{S}(\mathbf{u}_k + s^*\Delta\mathbf{u}_k)\cdot\Delta\mathbf{u}_k \mathrm{d}s^*\,, \end{cases} \tag{67}$$

with the integrand representing the incremental stress response associated with an incremental displacement step along the path.

In practice, we consider two numerical schemes for evaluating this integral: a forward Euler subiterative scheme and an implicit midpoint scheme.

Forward Euler

The forward Euler method with one integration step is the easiest integration scheme. The stress increment is estimated at the configuration obtained at displacement $\mathbf{u}_k$, for the whole increment of displacement $\Delta\mathbf{u}_k$.

$$\mathbf{S}_{k+1} = \mathbf{S}_k + \mathrm{D}\mathbf{S}(\mathbf{u}_k)\cdot\Delta\mathbf{u}_k\,. \tag{68}$$

A subiterative version of the forward Euler method is introduced by considering subdivision of the increment of displacement.

$$\mathbf{S}_{k+1} = \mathbf{S}_k + \sum_{j=0}^{m-1} \mathrm{D}\mathbf{S}\left(\mathbf{u}_k + j\frac{\Delta\mathbf{u}_k}{m}\right)\cdot\frac{\Delta\mathbf{u}_k}{m}\,, \tag{69}$$

with $m \in \mathbb{N}^*$ the number of subdivision steps. The proposed scheme does not require the inversion of the tangent matrix along with the subiterations. Accordingly, it is significantly faster than performing additional Newton Raphson steps, each with a one step explicit Euler integration scheme.

Implicit Midpoint

The other algorithm that we consider is an implicit midpoint algorithm. We follow the considerations of [21, 26] for the hypoelastic law based on the description of the Lie derivative. The stress increment is estimated at the configuration obtained by the displacement $\mathbf{u}_k + \alpha\Delta\mathbf{u}_k$, with $\alpha \in [0,1]$, reading:

$$\mathbf{S}_{k+1} = \mathbf{S}_k + \mathrm{D}\mathbf{S}(\mathbf{u}_k + \alpha\Delta\mathbf{u}_k) \cdot \Delta\mathbf{u}_k \,. \tag{70}$$

In this section and for the single-step implicit algorithm, the subscript $\mathbf{a}_{k+\alpha}$ denotes the value of any field $\mathbf{a}$ evaluated at $\mathbf{u}_k + \alpha\Delta\mathbf{u}_k$, where $\Delta\mathbf{u}_k$ is the increment of displacement. Then,

$$\begin{cases} \mathbf{F}_{k+\alpha} = \mathbf{1} + \nabla_{\mathrm{X}}(\mathbf{u}_k + \alpha\Delta\mathbf{u}_k) = \mathbf{F}_k + \alpha\nabla_{\mathrm{X}}\Delta\mathbf{u}_k \,, \\ \mathbf{d}_{k+\alpha} = \mathrm{Sym}\left(\nabla_{\mathrm{X}}(\Delta\mathbf{u}_k) \cdot \mathbf{F}_{k+\alpha}^{-1}\right) \,, \\ \mathrm{D}\mathbf{S}_{k+\alpha} = \mathrm{D}\mathbf{S}(\mathbf{u}_k + \alpha\Delta\mathbf{u}_k) \cdot \Delta\mathbf{u}_k = \mathbf{F}_{k+\alpha}^{-1} \cdot \mathcal{L}_v[\boldsymbol{\tau}]_{k+\alpha} \cdot \mathbf{F}_{k+\alpha}^{-T} \,, \\ \mathcal{L}_v[\boldsymbol{\tau}]_{k+\alpha} = \mathcal{L}_v[\boldsymbol{\tau}](\mathbf{u}_k + \alpha\Delta\mathbf{u}_k, \Delta\mathbf{u}_k) \,. \end{cases} \tag{71}$$

Estimating the increment of stress then depends on the constitutive law. For the Oldroyd derivative, the Lie derivative is independant from the stress field:

$$\mathcal{L}_v[\boldsymbol{\tau}]_{k+\alpha} = \mathbb{c} : \mathbf{d}_{k+\alpha} \,. \tag{72}$$

However, the other objective derivatives depend on the stress tensor estimated at $\mathbf{u}_k + \alpha\Delta\mathbf{u}_k$. For the Jaumann derivative, the increment of the Lie derivative reads:

$$\mathcal{L}_v[\boldsymbol{\tau}]_{k+\alpha} = \mathbb{c} : \mathbf{d}_{k+\alpha} - \boldsymbol{\tau}_{k+\alpha} \cdot \mathbf{d}_{k+\alpha} - \mathbf{d}_{k+\alpha} \cdot \boldsymbol{\tau}_{k+\alpha} \,. \tag{73}$$

Following [21], we introduce a one-parameter family of configuration, such that

$$\mathbf{S}_{k+\alpha} = \alpha\mathbf{S}_{k+1} + (1-\alpha)\mathbf{S}_k \quad , \quad \alpha \in [0,1] \,. \tag{74}$$

In this approach, the stress increment becomes implicit and depends on the stress value at the midpoint configuration.

$$\begin{aligned} &\mathbf{S}_{k+\alpha} = \mathbf{S}_k + \alpha\mathrm{D}\mathbf{S}_{k+\alpha} \,, \\ &\boldsymbol{\tau}_{k+\alpha} = \mathbf{F}_{k+\alpha} \cdot \mathbf{S}_{k+\alpha} \cdot \mathbf{F}_{k+\alpha}^T = \mathbf{F}_{k+\alpha} \cdot \mathbf{S}_k \cdot \mathbf{F}_{k+\alpha}^T + \alpha\mathcal{L}_v[\boldsymbol{\tau}]_{k+\alpha} \,. \end{aligned} \tag{75}$$

In this case, the increment of the Lie derivative is implicit. For the Jaumann derivative, it reads:

$$\begin{aligned} \mathcal{L}_v[\boldsymbol{\tau}]_{k+\alpha} = \mathbb{c} : \mathbf{d}_{k+\alpha} &- (\mathbf{F}_{k+\alpha} \cdot \mathbf{S}_k \cdot \mathbf{F}_{k+\alpha}^T) \cdot \mathbf{d}_{k+\alpha} - \mathbf{d}_{k+\alpha} \cdot (\mathbf{F}_{k+\alpha} \cdot \mathbf{S}_k \cdot \mathbf{F}_{k+\alpha}^T) \\ &- \alpha \left[\mathcal{L}_v[\boldsymbol{\tau}]_{k+\alpha} \cdot \mathbf{d}_{k+\alpha} + \mathbf{d}_{k+\alpha} \cdot \mathcal{L}_v[\boldsymbol{\tau}]_{k+\alpha}\right] \,. \end{aligned} \tag{76}$$

To solve this equation for $\mathcal{L}_v[\boldsymbol{\tau}]_{k+\alpha}$, we use an iterative approach. It is initialized with $\mathcal{L}_v[\boldsymbol{\tau}]_{k+\alpha}^0 = \mathbf{0}$ and while $||\mathcal{L}_v[\boldsymbol{\tau}]_{k+\alpha}^{i+1} - \mathcal{L}_v[\boldsymbol{\tau}]_{k+\alpha}^i|| > \epsilon_{int}$, it is updated as follow:

$$\begin{aligned} \mathcal{L}_v[\boldsymbol{\tau}]_{k+\alpha}^{i+1} = \mathbb{c} : \mathbf{d}_{k+\alpha} &- (\mathbf{F}_{k+\alpha} \cdot \mathbf{S}_k \cdot \mathbf{F}_{k+\alpha}^T) \cdot \mathbf{d}_{k+\alpha} - \mathbf{d}_{k+\alpha} \cdot (\mathbf{F}_{k+\alpha} \cdot \mathbf{S}_k \cdot \mathbf{F}_{k+\alpha}^T) \\ &- \alpha \left(\mathcal{L}_v[\boldsymbol{\tau}]_{k+\alpha}^i \cdot \mathbf{d}_{k+\alpha} + \mathbf{d}_{k+\alpha} \cdot \mathcal{L}_v[\boldsymbol{\tau}]_{k+\alpha}^i\right) \quad , \quad i \in \mathbb{N} \,. \end{aligned} \tag{77}$$

Once converged, the increment of the Lie derivative is directly used in Eqs. (70) and (71). The same process is used for the Green-Naghdi and the logarithmic derivatives. For the Green-Naghdi derivative, the incremental process reads:

$$
\begin{aligned}
\mathcal{L}_v[\boldsymbol{\tau}]_{k+\alpha}^{i+1} = \mathbb{c} : \mathbf{d}_{k+\alpha} &- (\mathbf{F}_{k+\alpha} \cdot \mathbf{S}_k \cdot \mathbf{F}_{k+\alpha}^T) \cdot (\mathbf{d}_{k+\alpha} + \boldsymbol{\Upsilon}_{k+\alpha}^{GN}) \\
&+ (\boldsymbol{\Upsilon}_{k+\alpha}^{GN} - \mathbf{d}_{k+\alpha}) \cdot (\mathbf{F}_{k+\alpha} \cdot \mathbf{S}_k \cdot \mathbf{F}_{k+\alpha}^T) \\
&+ \alpha \Big[- \mathcal{L}_v[\boldsymbol{\tau}]_{k+\alpha}^{i} \cdot (\mathbf{d}_{k+\alpha} + \boldsymbol{\Upsilon}_{k+\alpha}^{GN}) \\
&\qquad + (\boldsymbol{\Upsilon}_{k+\alpha}^{GN} - \mathbf{d}_{k+\alpha}) \cdot \mathcal{L}_v[\boldsymbol{\tau}]_{k+\alpha}^{i} \Big] \quad , \quad i \in \mathbb{N} \, .
\end{aligned}
\tag{78}
$$

Finally, for the logarithmic derivative, it reads:

$$
\begin{aligned}
\mathcal{L}_v[\boldsymbol{\tau}]_{k+\alpha}^{i+1} = \mathbb{c} : \mathbf{d}_{k+\alpha} &- (\mathbf{F}_{k+\alpha} \cdot \mathbf{S}_k \cdot \mathbf{F}_{k+\alpha}^T) \cdot (\mathbf{d}_{k+\alpha} + \boldsymbol{\Upsilon}_{k+\alpha}^{Log}) \\
&+ (\boldsymbol{\Upsilon}_{k+\alpha}^{Log} - \mathbf{d}_{k+\alpha}) \cdot (\mathbf{F}_{k+\alpha} \cdot \mathbf{S}_k \cdot \mathbf{F}_{k+\alpha}^T) \\
&+ \alpha \Big[- \mathcal{L}_v[\boldsymbol{\tau}]_{k+\alpha}^{i} \cdot (\mathbf{d}_{k+\alpha} + \boldsymbol{\Upsilon}_{k+\alpha}^{Log}) \\
&\qquad + (\boldsymbol{\Upsilon}_{k+\alpha}^{Log} - \mathbf{d}_{k+\alpha}) \cdot \mathcal{L}_v[\boldsymbol{\tau}]_{k+\alpha}^{i} \Big] \quad , \quad i \in \mathbb{N} \, .
\end{aligned}
\tag{79}
$$

For the Green-Naghdi and logarithmic derivatives, the spin rates $\boldsymbol{\Upsilon}_{k+\alpha}^{GN}$ and $\boldsymbol{\Upsilon}_{k+\alpha}^{Log}$ only depend on the displacement field and can be explicitly computed at $\mathbf{u}_k + \alpha \Delta \mathbf{u}_k$.

As for the Forward Euler integration algorithm, a sub-iterative version of the implicit midpoint scheme is implemented using a successive subdivision of the increment of displacement.

$$
\mathbf{S}_{k+1} = \mathbf{S}_k + \sum_{j=0}^{m-1} \mathrm{D}\mathbf{S} \left(\mathbf{u}_k + (j+\alpha) \frac{\Delta \mathbf{u}_k}{m} \right) \cdot \frac{\Delta \mathbf{u}_k}{m} \, ,
\tag{80}
$$

where the increment of stresses are computed thanks to the Eqs. (71) to (79) adapted for an increment of displacement $\dfrac{\Delta \mathbf{u}_k}{m}$.

In practice, a common choice for the implicit midpoint algorithm, adopted also in what follows, is $\alpha = 0.5$.

2.5.3 Code structure

Fig. 2 presents the structure of the Python code. The preprocessing stage defines standard finite element modeling steps (e.g., geometry, mesh, and material properties). It also includes the construction and pre-compilation of specific symbolic forms regarding the hypoelastic laws, their associated PKII stress rates, and the weak form adapted for a stress-rate formulation. The iterative process consists of three nested loops: stress integration, the Newton-Raphson solver, and temporal discretization.

The code is available publicly on GitHub at https://github.com/BastienSauty/FeniCSx-Hypoelasticity. We have included a Jupyter notebook as a minimal example to highlight how the equations developed formally in the paper are translated into practical numerical code. Specifically, the automatic differentiation tools of FEniCSx are utilized to derive the linear solver from the symbolic weak form representation. This ensures the consistent definition of the various finite-element fields driving the mechanical behavior.

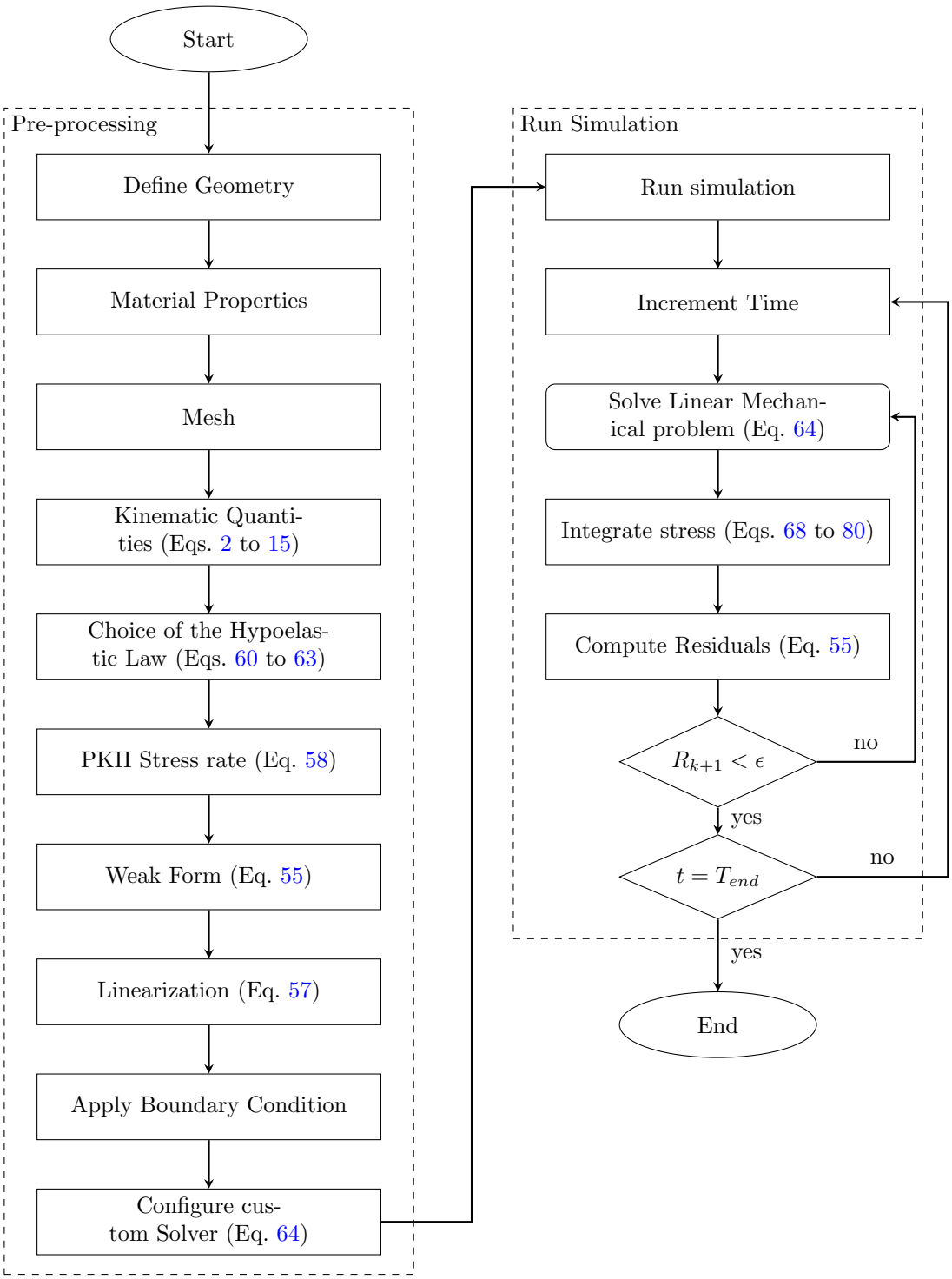

Fig. 2: Schematic representation of the numerical strategy

3 Benchmark cases: Numerical Results

This section presents the benchmark cases used to evaluate the performance of the proposed 3D finite element framework. Section 3.1 introduces a simple tensile–shear test on a single element, designed to assess the response of an individual material point. Section 3.2 then examines a plate with a central hole. Finally Section 3.3 investigates the response of a 3D Cook's membrane under complex loading conditions. Together, these examples enable a comprehensive assessment of the integration of the hypoelastic formulation within complex mechanical simulations. As shown by Lin [21], spurious energy generation becomes significant at high shear strains (above approximately 15%) and all of the benchmark cases considered here involve regions that experience such levels of shear deformation. The first three Sections address grade-zero hypoelasticity. Finally, Section 3.4 demonstrates how this numerical framework can be leveraged to explore novel hypotheses in finite strain modeling. Specifically, we apply the aforementioned benchmarks to a newly proposed consistent approach for Eulerian hyperelasticity, which extends the hypoelastic framework beyond the standard grade-zero case.

3.1 Grade-zero hypoelasticity: material point study

First, we verify the consistency of the framework with previous studies, with particular attention to the path-dependency arising from the choice of objective derivative, for grade-zero hypoelasticity. The analytical results from Lin [21] are reproduced in a numerical setting, addressing the combined tensile-shear test presented in Fig. 3. Lin [21], studied the path-dependency of different objective derivatives at the material point level. Hence we consider a simple mesh with one element and with linear displacement shape functions, to obtain homogenous constant stresses and strains. The material is chosen with a Young's modulus of $E = 30\,\mathrm{GPa}$ and a Poisson coefficient $\nu = 0.3$, such that the Lamé coefficients are: $\mu = 11.5\,\mathrm{GPa}$ and $\lambda = 17.3\,\mathrm{GPa}$. The out-of-plane surfaces are constrained with a Dirichlet boundary condition, such that $u_x = 0$. The maximum displacements applied are $u_y/L = u_z/L = 0.5$, such that the maximum shear and tensile strains applied are of 50%. Fig. 3 presents the boundary conditions and loading path.

3.1.1 Single element behavior under combined tensile-shear stress

In their study, Lin [21] studied this benchmark using a Eulerian approach of the material point problem. Using the developed Finite Element Framework, we reproduce their results, ensuring the consistency of our full Lagrangian FEM. Fig. 4 shows the evolution of the components of the Cauchy stress during the different steps of successive loadings for the four considered objective derivatives of the Kirchhoff stress: Oldroyd, Jaumann, logarithmic and Green-Naghdi. These results highlight the impact of the choice of objective derivative on the behavior of a single material point and in this case on a single element. The most significant difference can be observed for the Oldroyd rate (fig. 4a), both regarding the values attained after loading and the creation of residual stresses. The Jaumann and Green-Naghdi stress rate (fig. 4b and

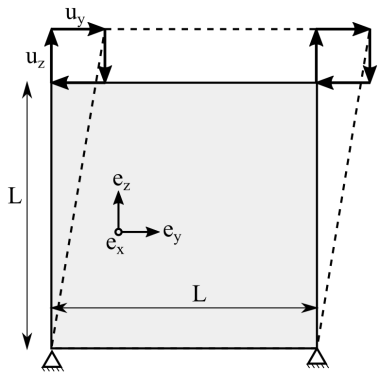

(a) Geometry and boundary conditions

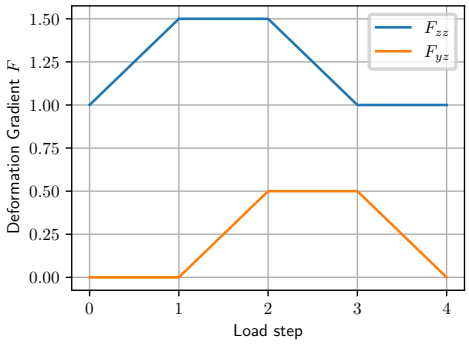

(b) Path of deformation

Fig. 3: Combined Shear-Tensile test, adapted from [21]. Fig. a and b respectively recall the geometry and boundary condition and the loading path.

4c) present some residual stresses. Only the logarithmic derivative (fig. 4d) does not present any residual stress.

3.1.2 Temporal discretization and stress integration

Even though Fig. 4d does not show evident residual stresses for the logarithmic objective derivative, the stress-rate hypoelastic formulation relies on the successive integration of the stress rate. Hence, some numerical errors are bound to appear in the simulations. In this benchmark problem, the numerical inaccuracy arises from the integration part in the resolution of the mechanical equilibrium rather than the spatial discretization. Fig. 5 presents the evolution of the normalized residual stress depending on the number of Newton-Raphson steps and the number of subiterations for the stress integration, using the Forward Euler integration scheme.

Whereas Fig. 5a shows that the temporal discretization has a small impact on the residual stresses, Fig. 5b shows that the subiteration process improves the accuracy of the stress integration and thereof reduces the residual stresses. The residual stresses converge toward plateau values that are inherent to the formulation of the objective derivatives.

Overall, Fig. 5 highlights the importance of a proper stress integration scheme in a hypoelastic formulation. The temporal discretization has a limited impact on the accuracy of the stress computation. Conversely, the number of subiterations chosen in the stress integration algorithm is crucial in the accuracy and the creation of residual stresses. Indeed, even for the logarithmic derivative, a 4.5% error would arise from an explicit Euler integration scheme. When considering 20 steps for the stress integration, the error becomes lower then 1%.

Fig. 6 present the same sensitivity analysis, using the implicit Midpoint scheme presented in sec. 2.5.2. Fig. 6b shows that the errors are dominated by the theoretical formulation, rather than the numerical integration scheme. The self-consistent nature

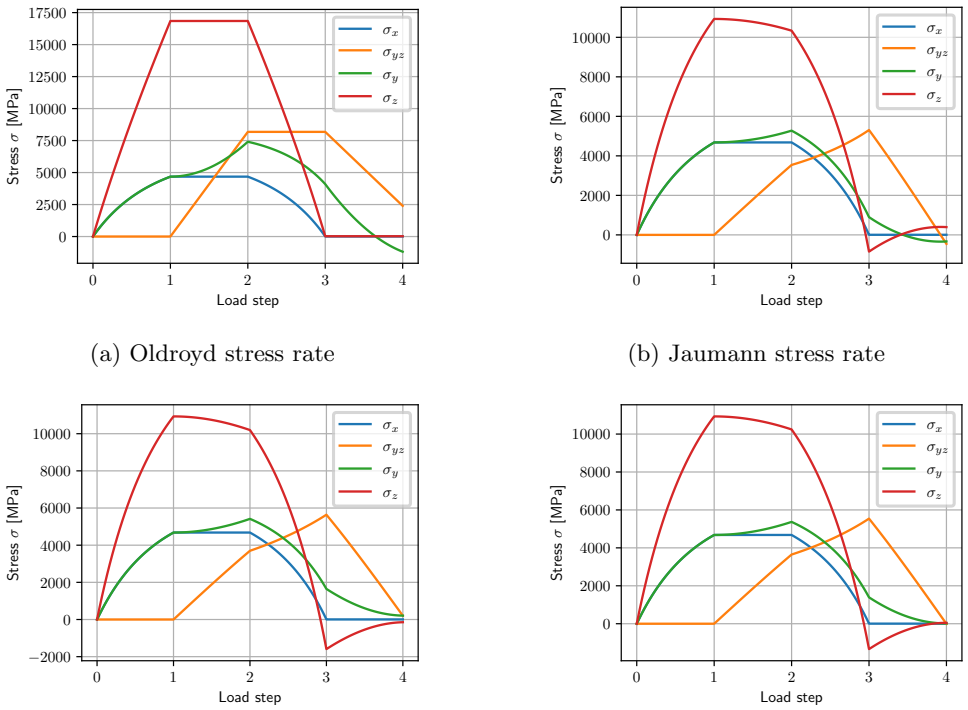

(a) Oldroyd stress rate

(b) Jaumann stress rate

(c) Green-Naghdi stress rate

(d) Log stress rate

Fig. 4: Stress curve for the shear-tensile test reproducing [21], with $\mu = 11.5$GPa and $\lambda = 17.3$GPa

of this scheme makes it much more precise, making the use of subiterations useless. This accuracy comes at a computational price, as the midpoint integration scheme is slower (see Fig. 7). However, since multiple subiterations (> 30) are required to reach a converged value with the forward Euler scheme and no subiteration is necessary with the implicit midpoint scheme, the latter is more competitive than the former in this material point case study.

3.2 Grade-zero hypoelasticity: plate with a hole

In order to analyze the effect of different grade-zero hypoelastic laws in scenarios closer to real-world structures, we analyze a plate with a central hole subjected to biaxial tension. This setup provides a relevant benchmark for examining the response of a structure with complex stress fields, since an equibiaxial state far from the hole couples with significant shear stress states around the hole. In particular, we analyze the residual strains that develop in such a structure using different objective stress rates.

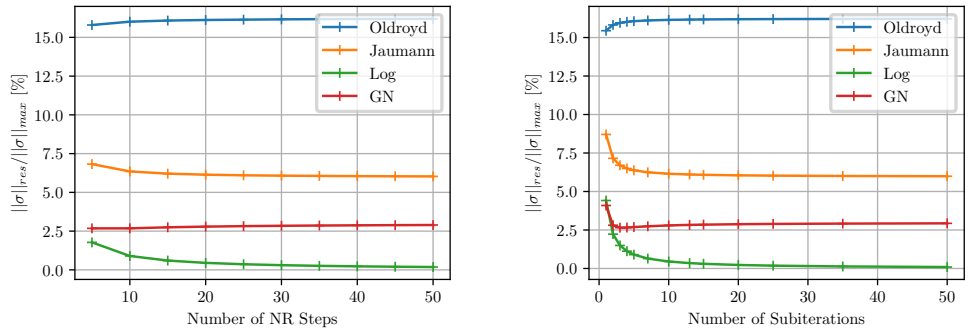

(a) Residual stresses as a function of load step discretization for 25 subiterations

(b) Residual stresses as a function of subiterations for 50 NR steps

Fig. 5: Impact of the number of load steps and number of subiterations on the evolution of Residual Stresses, using the Forward Euler scheme

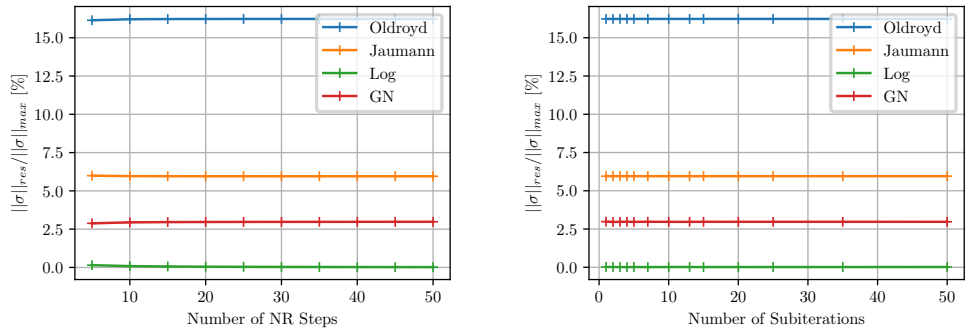

(a) Residual stresses as a function of load step discretization for 1 subiteration

(b) Residual stresses as a function of subiterations for 50 NR steps

Fig. 6: Impact of the number of load steps and number of subiterations on the evolution of Residual Stresses, using the Implicit Midpoint scheme

The plate is $L = 5\,\text{mm}$ large and $h = 1\,\text{mm}$ thick with a hole of radius $R = 1\,\text{mm}$. We plot in Fig. 8 the geometry and boundary conditions. To reduce computational time, only a quarter of the geometry is considered, through the application of symmetric boundary conditions. A successive biaxial load is applied through Dirichlet boundary conditions with successive and progressive displacements u_x and u_y, shown in Fig. 8b. This 3D geometry is loaded in a plane stress configuration through two boundary conditions on the top and bottom faces. A symmetry condition $u_z(z = 0) = 0$ is applied on the bottom face, while the top face is stress free, that is $\sigma_{zz}(z = h) = 0$.

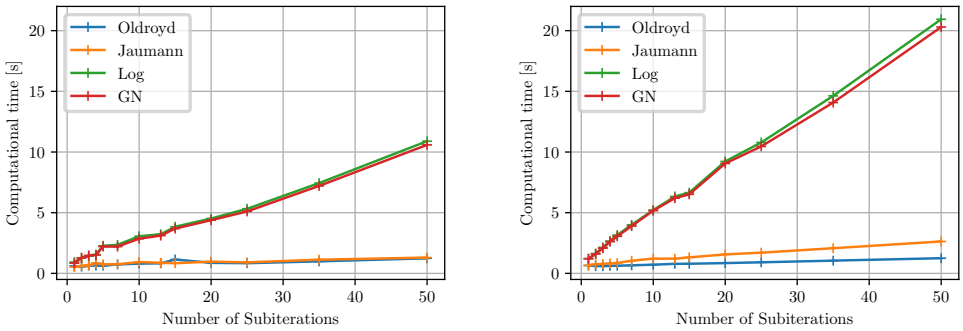

(a) Forward Euler algorithm (b) Implicit Midpoint algorithm

Fig. 7: Computational cost for the different integration scheme

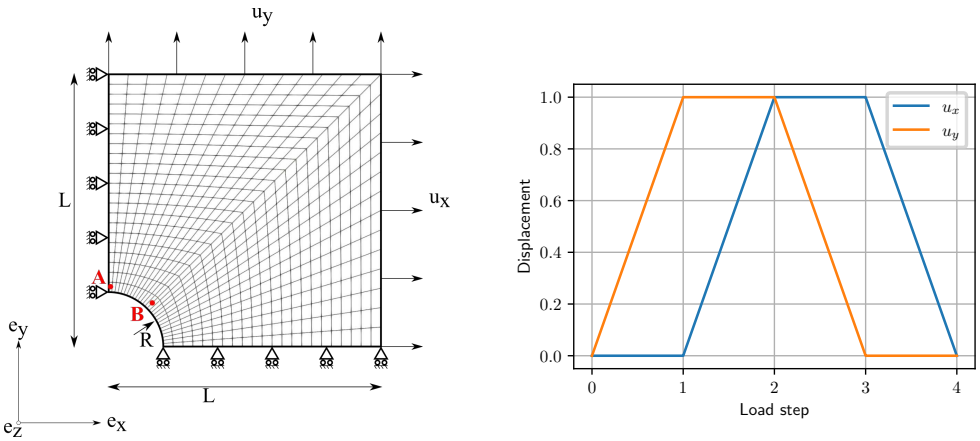

(a) Geometry and boundary conditions (b) Deformation path

Fig. 8: Plate with a hole loaded by a biaxial tensile test. Fig. a presents the considered geometry with a 0.2 mm fine mesh. Symmetry boundary conditions are chosen to reduce computational time. The local mechanical behavior of the structure is examined at designated points A and B, corresponding to the locations of maximum tensile and shear strain, respectively.

The mesh is 3D hexahedral. If not differently specified, the elements have a characteristic size of 0.2 mm, for a total number of 1334 elements. We verified that the number of elements on the thickness has no effect on the results due to the plane-stress configuration. In this study, we use one element in the thickness so as to reduce the computational time.

An aggregated measure of the stress is used to study the overall error of the numerical framework for the whole structure. The aggregated stress measure is defined

using the L2-norm of the stress tensor, see Eq. (81). The local behavior of the finite element model is studied at two critical points in the structure: points A and B, as defined in Fig. 8a. These points are chosen because they experience the maximum tensile and shear strain within the structure, respectively.

$$||\mathbf{S}|| = \sqrt{\frac{1}{\mathrm{V}_0}\int_{\mathcal{B}_0} \mathbf{S} : \mathbf{S}\,\mathrm{dV}} \tag{81}$$

Sect. 3.2.1 presents the mechanical response of the structure with the different objective derivatives. Then in Sect. 3.2.2, the sensitivity of the model to numerical parameters is studied, specifically the influence of the subintegrations steps and the mesh size. Finally, Sect. 3.2.3 presents the response of the structure to a repeated cyclic load.

3.2.1 Analysis of the mechanical response

A first simulation is made using the fine mesh, the logarithmic derivative and fine integration parameters (50 subintegrations and 50 steps per load step). The biaxial load applied on the plate leads to an average tensile strain of 18% and a shear strain of 3.5%. Fig. 9 presents the evolution of the average mechanical quantities during biaxial loading. In this structure, the mechanical state is predominantly a tensile strain, however the hole affects its surrounding mechanical state, through a shear strain. The mechanical state at maximal load (step 2) is presented Fig. 10. Around the hole, a maximal shear strain of 36% is obtained. Hence, this is a case where the Jaumann derivative might create non-negligible residual stresses.

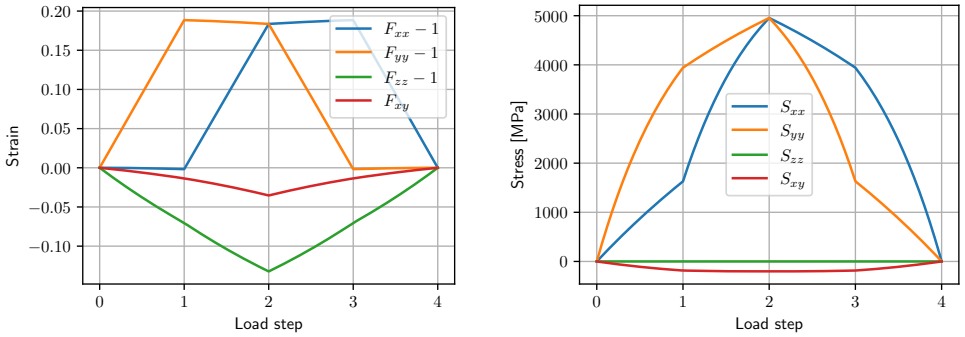

(a) Average strain

(b) Average PKII stress

Fig. 9: Average mechanical state during biaxial tensile test: strain (a) and stress (b)

Fig. 11 presents the residual Von Mises stresses observed after successive loading and unloading cycles for the different objective derivatives. The chosen objective derivative affects not only the magnitude but also the spatial distribution of these residual stresses. The Oldroyd derivative (Fig. 11a) leads to high residual stresses

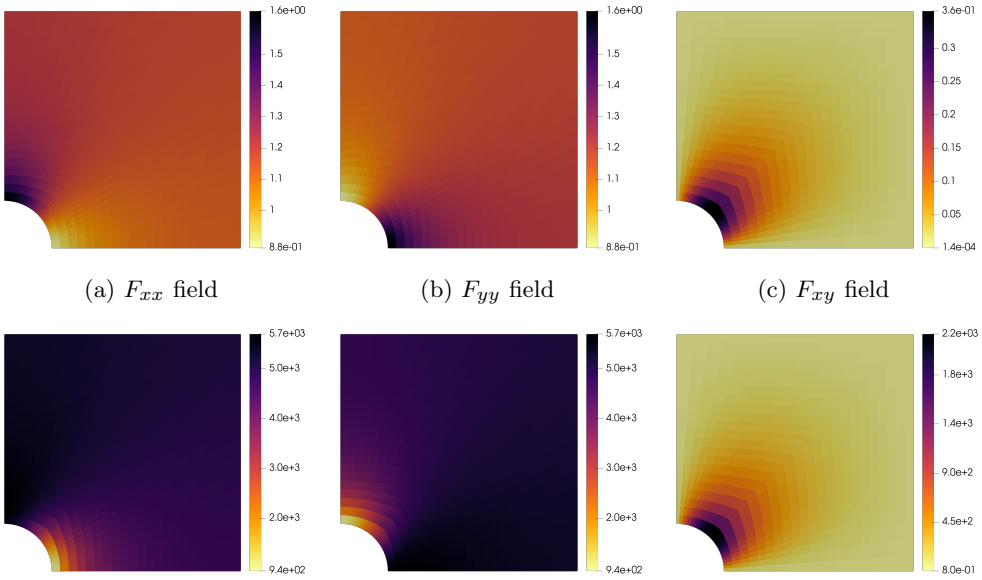

(a) F_{xx} field (b) F_{yy} field (c) F_{xy} field

(d) σ_{xx} field [MPa] (e) σ_{yy} field [MPa] (f) σ_{xy} field [MPa]

Fig. 10: In plane mechanical state at maximum load (step 2) using the logarithmic derivative. Panels a, b and c display the components of the deformation gradient. Panels d, e and f display the components of the stress tensor.

distributed throughout the entire structure. In contrast, the Jaumann (Fig. 11b), Green-Naghdi (Fig. 11c) and logarithmic (Fig. 11d) derivatives result in stress concentrations primarily around the hole. Locally, the errors associated with the Jaumann derivative are twice as large as those from the Green-Naghdi derivative, which are themselves ten times greater than those from the logarithmic derivative. Nevertheless, some residual errors persist for the logarithmic derivative, arising from the numerical framework.

3.2.2 Influence of the numerical parameters

As for the simple combined tensile-shear test in Sect. 3.1.1, the numerical scheme plays a critical role in the creation of residual stresses. The temporal discretization, as observed in Sect. 3.1.2, has a limited influence on the overall results, so it is fixed here at 50 steps per load step. In this section we study the influence of the number of subintegration steps and of the spatial discretization, that is the mesh quality, on the residual stresses. The residual stresses are measured through the L2-norm of the Cauchy stress as defined in Eq. (81).

The influence of the integration algorithm through the number of subiteration is presented in Fig. 12a. This sensitivity analysis is done using a fine mesh. Results are normalized by the maximal norm of the stresses attained at step 2. This figure highlights the crucial role of the integration algorithm for the global accuracy of the

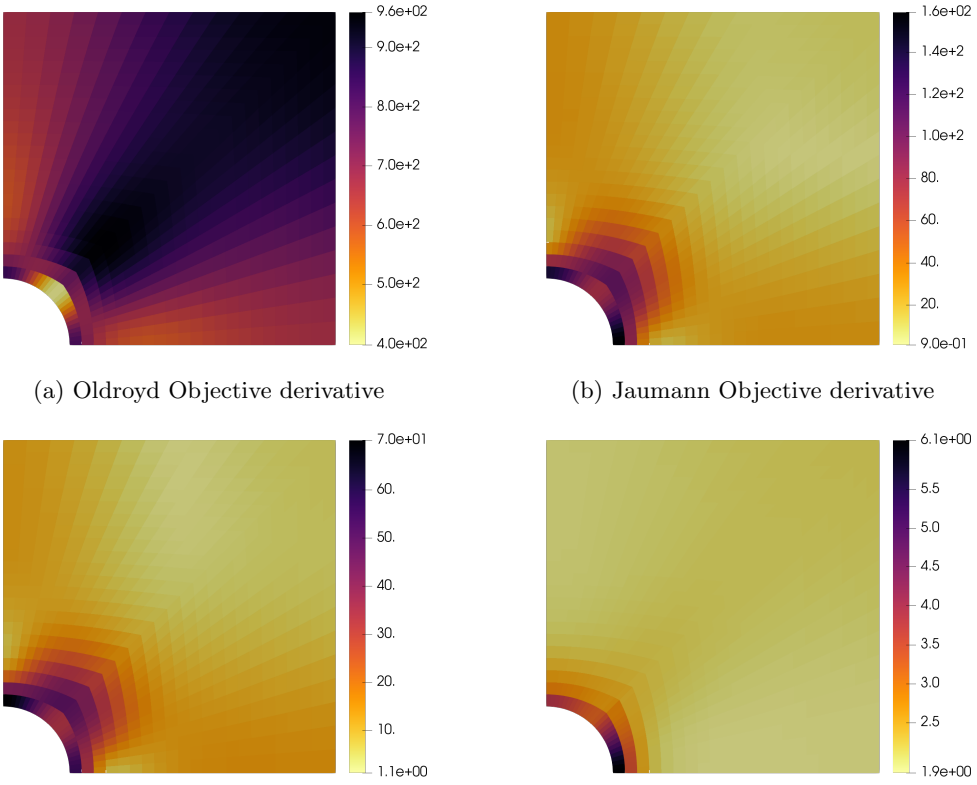

(a) Oldroyd Objective derivative

(b) Jaumann Objective derivative

(c) Green-Naghdi Objective derivative

(d) logarithmic Objective derivative

Fig. 11: Von Mises magnitude [MPa] of the residual stresses after one biaxial successive loading of the plate with a hole, considering the different objective derivatives.

whole structure model. Conversely, the size of the elements shows little impact on the creation of residual stresses. Fig. 12b presents the evolution of residual stresses for meshes with a characteristic size varying from 0.1 mm to 0.5 mm for a plate width of $L = 5$ mm. The results show that the mesh density has negligible influence on the accumulation of residual stress, highlighting the stability of the implementation.

This sensitivity analysis reinforces the conclusion in Sect. 3.1.1: the integration algorithm is the most crucial ingredient for the accuracy of the hypoelastic models.

As for Sect. 3.1.1, the implicit midpoint integration scheme presents significantly more accurate results. Fig. 13 displays the evolution of residual stresses in the structure for the different sets of numerical parameters. Using the midpoint integration scheme, numerical errors arise mostly from the theoretical formulation of the constitutive law. However this accuracy comes at a computational cost, as shown in Fig. 14. In this case, the forward Euler scheme with a sufficient number of subiterations (more than 30) proves to be more efficient than the implicit midpoint rule without sub-iterations. Specifically, the computational time for the forward Euler method is approximately

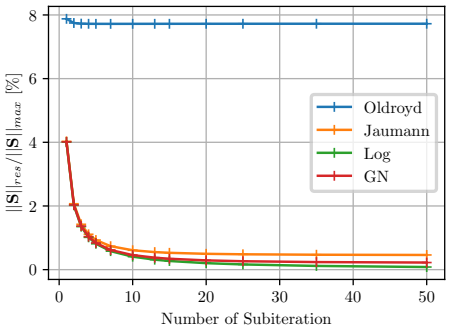

(a) Influence of the subiterations, for a $0.2mm$ mesh

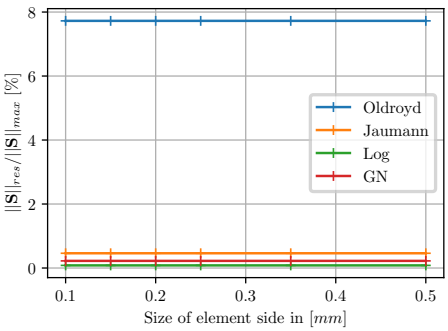

(b) Influence of the mesh size, with 50 subiterations

Fig. 12: Impact of the numerical parameters on Residual Stresses using the Forward Euler integration scheme: number of subiterations (a) and mesh size (b).

350 seconds, compared to around 450 seconds for the implicit midpoint rule. As a result we obtain a reduction of 25% in computational cost.

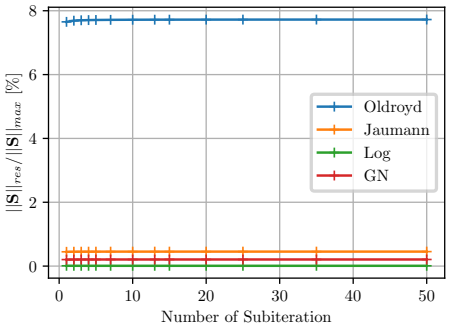

(a) Influence of the subiterations, for a $0.2mm$ mesh

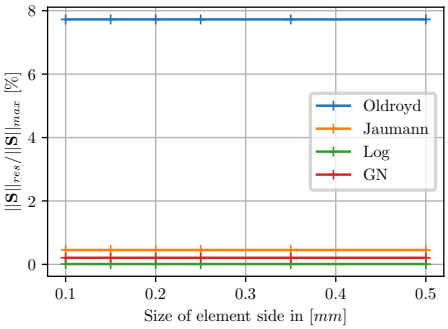

(b) Influence of the mesh size, with 50 subiterations

Fig. 13: Impact of Numerical Parameters on Residual Stresses using the Implicit Midpoint integration scheme: number of subiterations (a) and mesh size (b).

3.2.3 Repeating a cyclic loading: accumulation of spurious residual stresses

The spurious residual stresses reported in the previous section accumulate when the structure is cyclically loaded. This leads to a drift in the stress measure for the unloaded configuration, but also during loading.

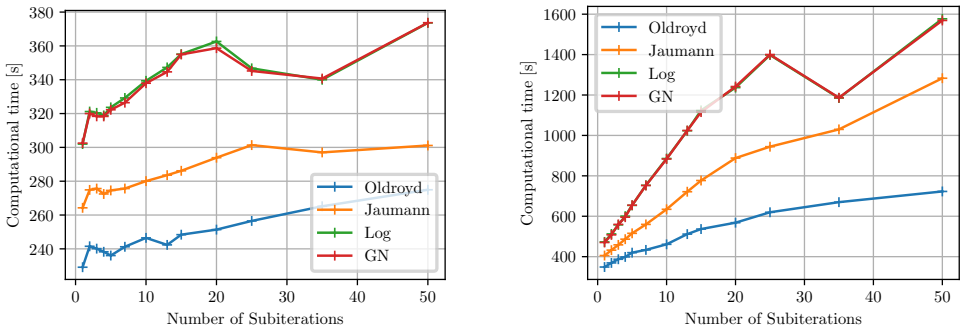

(a) Forward Euler algorithm

(b) Implicit Midpoint algorithm

Fig. 14: Computational cost for the different integration schemes. While the overall trend is monotonic with the increase of subiterations, localized fluctuations in wall-clock time reflect hardware-level execution variability within the FEniCSx/PETSc environment.

In this section we simulate 20 cycles of successive biaxial load on the plate. The mesh is $0.2mm$ fine and we use the Forward Euler integration scheme with 50 subiterations and 50 temporal steps per load steps. Fig. 15 presents the evolution of the residual stresses after each cycle for the different objective derivative. In this figure, the norm of the stress tensor is normalized by its maximal value attained at step 2. The theoretical value is unknown, hence we compute it at the first cycle of loading using the logarithmic derivative. It is denoted $||\mathbf{S}||^{log,1}_{max}$ and it is taken as the fiducial value of maximal stress.

Fig. 15a shows that the accumulation of residual stresses is linearly dependent on the number of cycles. The Oldroyd derivative accumulates stresses rapidly, gaining up to 80% error in 10 cycles. This makes it unstable and divergent and we chose to ignore it for the rest of the study. Fig. 15b presents the same results with a focus on the Jaumann, Green-Naghdi and logarithmic derivatives. This shows that even if the errors are initially low, they can rise up to significant value after a limited number of cycles. The Jaumann derivatives presents up to 8% error after only 20 cycles.

Locally, the errors are even more important, especially around the hole, as this is the region with the most important shear strain. Fig. 16 presents the evolution of the maximal stresses and residual stresses for each cycles at two different points in the mesh. Points A and B are defined in Fig. 8a and are chosen as the points during loading that undergo the maximal tensile strain (point A) and maximal shear strain (point B). The stresses, respectively tensile (Fig. 16a and 16b) and shear (Fig. 16c and 16c) are normalized by the maximal respective tensile and shear stresses attained at step 2, for the first cycle of loading using the logarithmic derivative, denoted $\boldsymbol{\sigma}^{log,1}_{yy,max}$ and $\boldsymbol{\sigma}^{log,1}_{xy,max}$.

Fig. 16a and 16b shows that the tensile stress at point A is undergoing significant drift for the Jaumann (40% error) and Green-Naghdi (10% error) derivative. This

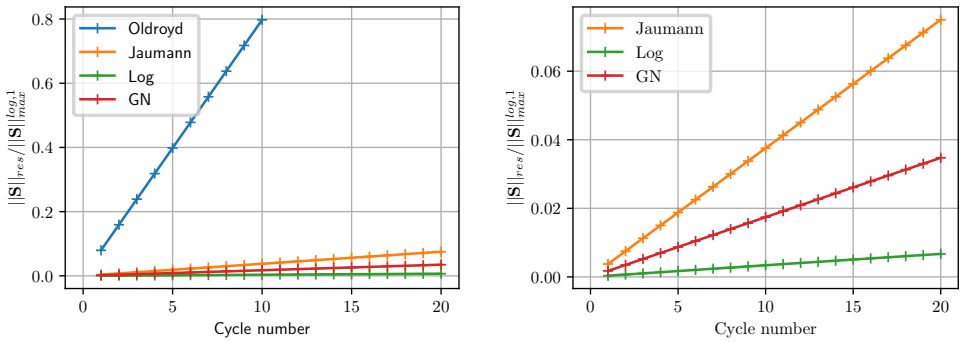

(a) Norm of the residual stresses

(b) Zoom without the Oldroyd results

Fig. 15: Evolution of the residual stresses for the repetition of the cyclic loading. Fig. a shows the important drift of the Oldroyd objective derivative. Fig. b focus on the Jaumann, Green-Naghdi and logarithmic results.

highlights the impact of residual stresses, not only in the unloaded configuration but also on the loaded state.

Fig. 16c and 16d present the shear stress at point B. This also undergoes significant drift for the Jaumann derivative, with a 10% error at maximum stress and a 4% error in the residual stress.

Overall this study highlights the critical role of residual stress accumulation when considering cyclic loading. Even for the theoretically exact logarithmic stress rate, the numerical scheme and particularly the stress integration scheme are of paramount importance for the accuracy of a stress rate constitutive model.

3.3 Grade-zero hypoelasticity: 3D Cook's membrane problem

The present framework is designed for complex three-dimensional boundary value problems. While the previous test cases were restricted to plane loading conditions, the Cook Membrane serves as a benchmark for geometrically nonlinear structures subjected to mixed in-plane and out-of-plane shear for grade-zero hypoelastic laws. This use-case therefore extends the scope of the validation to slender structures experiencing bending, rotation and buckling.

The membrane geometry corresponds to the classical Cook configuration, extruded to a thickness of 5 mm and discretized with five elements across the thickness. To avoid the well-known locking issues associated with bending-dominated problems like Cook's membrane, a structured hexahedral mesh was employed, ensuring the focus remains on the constitutive response and rate integrability. The geometry is presented in Fig. 17a. The left surface is clamped and a follower load is applied on the opposite surface as a Neumann boundary condition. The applied traction vector combines two shear components: an in-plane shear T_y and an out-of-plane shear T_z. The load is applied following an asymmetric shear cycle, illustrated in Fig. 17b. Stress integration

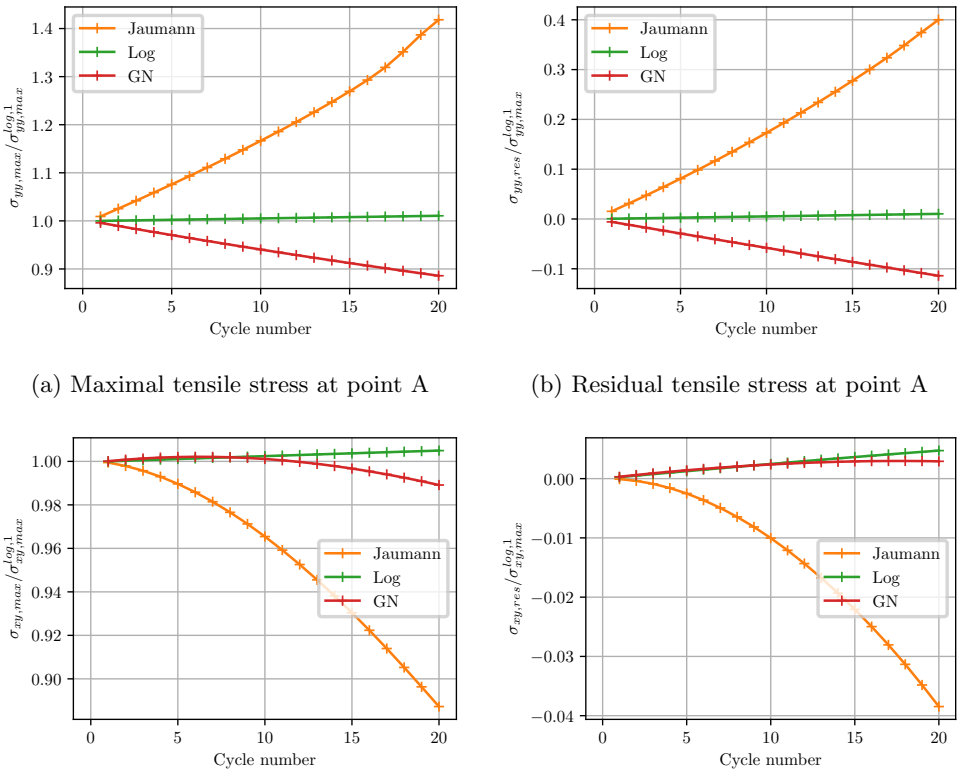

(a) Maximal tensile stress at point A

(b) Residual tensile stress at point A

(c) Maximal shear stress at point B

(d) Residual shear stress at point B

Fig. 16: Local behavior of the structure under repeated cycling. Fig. a and b present the residual and maximum tensile stresses observed at point A. Fig. c and d present the residual and maximum shear stresses observed at point B. These points are defined in Fig. 8a.

is performed using an Euler scheme with 30 substeps and results are compared across different objective stress rates (Jaumann, Green–Naghdi and logarithmic).

Fig. 18a shows the deformed configuration at maximum load (step 2). The global deformation is dominated by out-of-plane bending rather than pure shear, which is consistent with the slenderness of the structure. Fig. 18b shows the trajectory of a representative control point, located on the upper-right loaded corner. The trajectory confirms a complex but reversible deformation path, with the structure recovering its initial position at the end of the cycle.

During the last unloading step (3→4), where only in-plane shear is present, a local out-of-plane displacement develops due to buckling of the membrane. This response depends on the structural geometry and loading rather than on the choice of constitutive model. Indeed, the same qualitative behavior was obtained with all objective stress rates as well as with a hyperelastic reference model (not shown here).

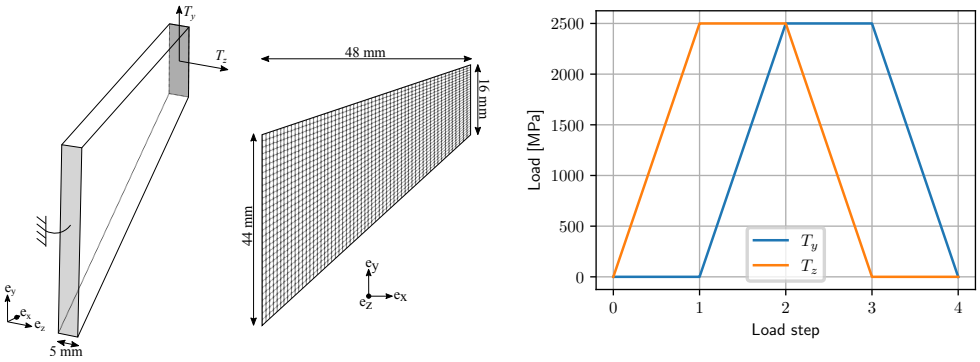

(a) Geometry and boundary conditions.

(b) Asymmetric shear load cycle.

Fig. 17: Cook Membrane configuration and applied loading. The traction vector is a follower load pulled back to the reference configuration.

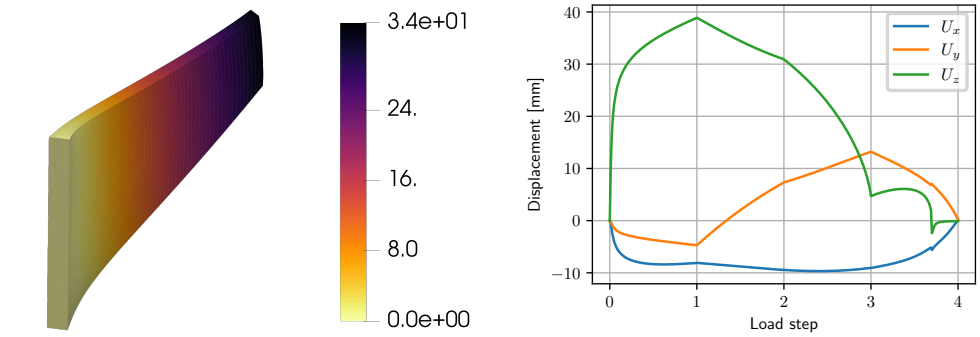

(a) Displacement magnitude in [mm] at maximum load (step 2).

(b) Displacement trajectory of the upper-right loaded point.

Fig. 18: Deformation of the Cook Membrane under combined shear, using an hypoelastic law based on the logarithmic rate. The global response is dominated by out-of-plane bending and in-plane shear. During the final unloading phase ($3 \rightarrow 4$), the membrane exhibits a local out-of-plane displacement U_z corresponding to a buckled equilibrium state. This phenomenon arises from compression induced by the shear state and is a physical consequence of the structural slenderness. This response is independent of the constitutive framework, as the same qualitative behavior was consistently observed for all objective stress rates and validated against a reference hyperelastic model (results not shown).

The strain distribution is shown in Fig. 19 for load steps 1 and 2. The E_{xz} shear strain highlights that local shear does develop, but the overall deformation is governed by bending and rotations.

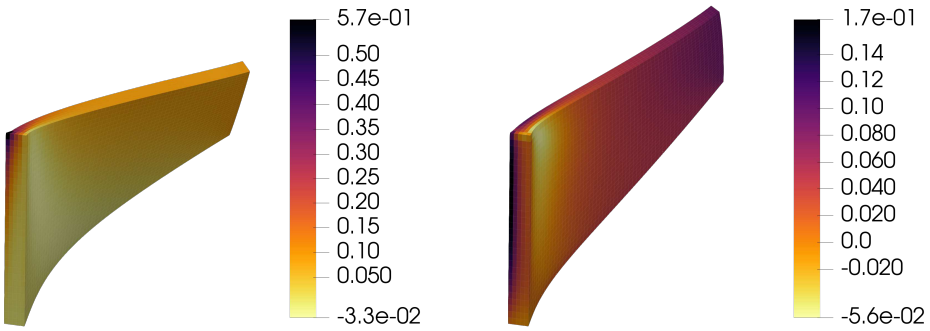

(a) Step 1 (b) Step 2

Fig. 19: E_{xz} shear strain at load step 1 and 2, respectively Panel a and b.

To further quantify the influence of the constitutive formulation, the residual stress state was evaluated at the end of the loading cycle. Although the Cook Membrane largely recovers its unloaded configuration, small residual von Mises stresses remain, depending on the choice of objective derivative. The normalized residual stresses are presented in Fig. 20. The results are normalized with respect to the maximum value of the Von Mises stress obtained in the whole body during loading, that is at the end of step 2. Similarly to the previous benchmarks (single element and plate with hole), the Cook Membrane shows small but measurable differences between formulations. At the end of the cycle, residual stresses range from approximately 0.23% for the logarithmic rate to 1.6% for the Jaumann rate.

The magnitude of these residuals is consistent with the errors observed in the plate-with-hole case, despite the fact that the Cook Membrane is subjected to a more complex deformation pattern combining bending, out-of-plane shear and buckling. This uniformity across varied configurations underscores the robustness of the proposed numerical framework. Specifically, the results suggest a stable implementation, as each objective stress rate yields comparable error magnitudes regardless of the problem geometry. Such stability is maintained even in the presence of buckling and follower loads, indicating that the chosen rates do not trigger uncontrolled spurious energy within the investigated regimes.

3.4 Beyond grade-zero hypoelasticity: a numerical study

In the previous sections, we established benchmark tests to assess the integrability of hypoelastic rates and their ability to prevent the generation of spurious energy and we applied them in the case of grade-zero hypoelasticity. We now apply this numerical framework to validate the approach for non-constant Eulerian stiffness matrices introduced in Sect. 2.4. This formulation systematically derives the stiffness matrix from an Exponentiated Hencky (EH) Eulerian hyperelastic potential using automatic differentiation in FEniCSx, integrated via the logarithmic objective derivative. To evaluate

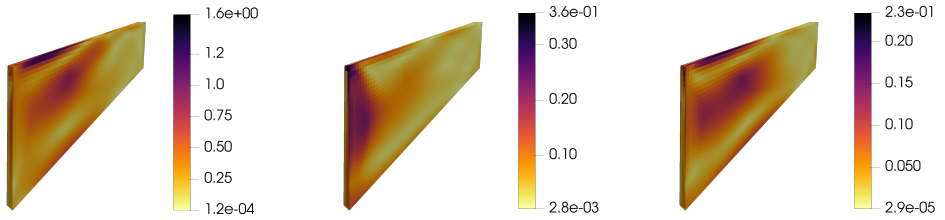

(a) Jaumann derivative (b) Green-Naghdi derivative (c) Logarithmic derivative

Fig. 20: Normalized residual von Mises stresses after the load cycle (in %), for the Jaumann (a), Green–Naghdi (b) and logarithmic (c) stress rates. The results are normalized with respect to the maximum value of the Von Mises stress obtained in the whole body during loading, that is at the end of step 2.

the performance and robustness of this non-linear model, we apply the three established benchmark cases using material parameters $\mu = 11.5\,\text{GPa}$, $\lambda = 17.3\,\text{GPa}$, and non-linear parameters $(k, \hat{k}) = (2, 2)$.

3.4.1 Tensile-Shear analysis

The cyclic tensile-shear test introduced in Sect. 3.1 is applied to the Exponentiated Hencky energy. Results are presented in Fig. 21a. The formulation demonstrates consistent physical behavior, as the stress returns exactly to zero at the end of the loading cycle. This absence of residual stress confirms that the proposed approach to constructing a non-constant stiffness matrix is numerically integrable and path-independent. Furthermore, the results highlight a distinct non-linear response compared to classical formulations, confirming that the EH energy successfully introduces a strain-dependent stiffness without compromising the consistency of the Eulerian rate-form.

3.4.2 Biaxial loading: plate with a hole

The stability of the Exponentiated Hencky formulation in non-homogeneous deformation fields was evaluated using the plate with a hole benchmark introduced in Sect. 3.2 (Fig. 21b). Using a Forward Euler integration scheme with 25 substeps, the model exhibited a residual error of 0.43%. This error magnitude is comparable to those observed for standard constant-stiffness objective rates, such as the Jaumann derivative (0.48%).

Given that the previous tensile-shear test proved the model's theoretical integrability, the residual error is attributed to the numerical complexity of integrating a rapidly evolving stiffness matrix rather than a constitutive deficiency. These results showcase the model's ability to represent highly non-linear material behavior in complex geometries while maintaining numerical stability.

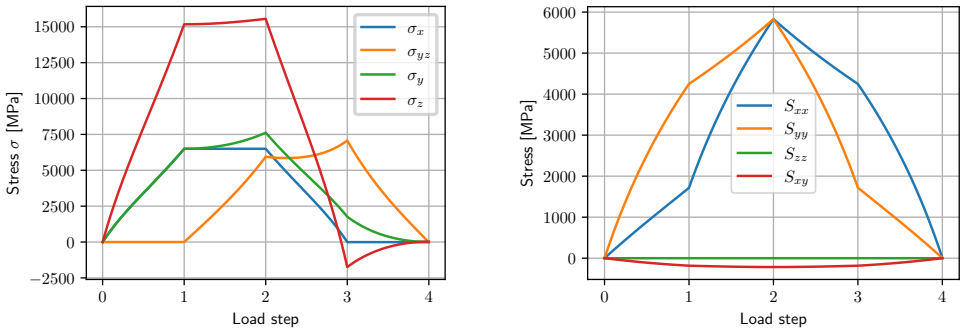

(a) Tensile-shear response

(b) QPH stress distribution

Fig. 21: Numerical study for the Exponentiated Hencky (EH) model ($(k, \hat{k}) = (2, 2)$). a) Verification of numerical integrability via the tensile-shear test introduced in Sect. 3.1. b) Stability in a non-homogeneous deformation field via the plate test introduced in Sect. 3.2.

3.4.3 3D Cook's membrane problem

Finally, the EH model was applied to the 3D Cook's Membrane benchmark (introduced in Sect. 3.3) to assess its performance in slender, shear-dominated geometries. As shown in Fig. 22a, the deformation path remains consistent with structural expectations for this geometry. The residual error field, presented in Fig. 22b, indicates that the Eulerian hyperelastic approach does not generate more spurious energy than standard constant-stiffness approaches. The error levels are of the same magnitude as those observed in the grade-zero case, confirming that the use of a non-constant stiffness matrix integrated via the logarithmic derivative provides a robust and consistent framework for finite strain analysis.

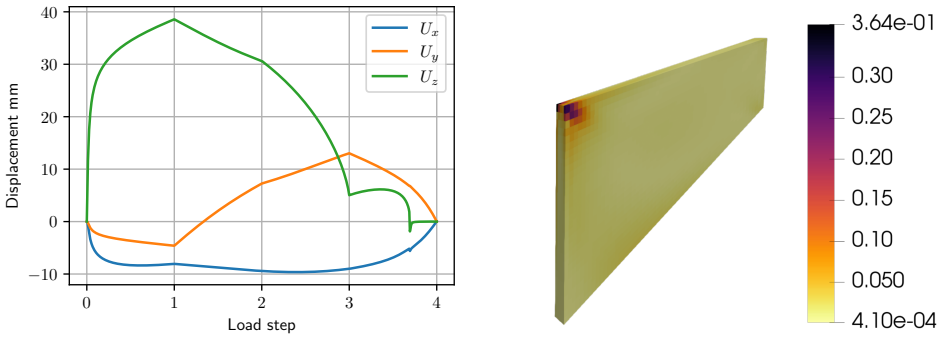

(a) Displacement vectors

(b) Normalized residual stress field

Fig. 22: 3D Cook's Membrane benchmark test introduced in Sect. 3.3 for the Exponentiated Hencky energy. a) Displacement vectors at peak load. b) Normalized residual Von Mises stress field after a full load-unload cycle, demonstrating that the non-constant stiffness formulation maintains the same level of numerical accuracy as classical hypoelastic models.

4 Discussion and conclusion

In this work, we have implemented hypoelastic constitutive models within a fully Lagrangian formulation. A particular emphasis was placed on the distinction between theoretical and numerical integrability. A consistent numerical strategy was developed and implemented in FEniCSx, based on the explicitly linearized weak form of mechanical equilibrium and solved via a Newton-Raphson algorithm. This framework enables the direct incorporation of stress-rate constitutive laws into the solver, while offering a reproducible and extensible open-source finite element implementation. Two dedicated stress integration schemes – a forward Euler algorithm and an implicit midpoint algorithm – were introduced and compared, together with a sub-iterative method that improves numerical accuracy at limited computational cost. Benchmark tests were further proposed to assess the effective error introduced by inadequate theoretical or computational formulations under varying loading conditions, thereby providing a systematic basis for verifying path independence in boundary value problems. Finally, we demonstrated the utility of this framework by investigating a non-constant Eulerian stiffness matrix derived from an energy potential. This case study serves to evaluate the numerical integrability of such a formulation and highlights the framework's capacity to handle advanced, energy-based hypoelastic laws.

Using FEniCSx proves to be a powerful and flexible tool, offering fine-grained control over the weak formulation of the equilibrium, solver configuration and stress integration strategy. In this work, we compared the Forward Euler scheme and implicit midpoint schemes, adapted for a Lagrangian approach. The implicit midpoint scheme proved to be more accurate and self-consistent, but its theoretical and computational complexity makes it less attractive in practice. By contrast, the forward Euler scheme remains simple and computationally efficient when the implicit formulation of the stress increment is more complex, e.g in hypoplasticity, or multiscale models. In this cases, a subiterative forward Euler scheme could be preferred to reduce both numerical errors and computational time. Consequently, we suggest that while the implicit midpoint scheme is ideal for simple constitutive laws where accuracy is paramount, a sub-iterative forward Euler scheme is often more practical for complex formulations. The proposed subiteration scheme achieves negligible numerical errors without requiring second-order accurate integration methods, such as the implicit midpoint rule. This leads to a significant reduction in computational effort when solving the boundary value problems addressed in this study. Interestingly, such efficiency gains are not evident in numerical tests at the material point level. This highlights how numerical and theoretical aspects can interact in nontrivial ways – emphasizing the importance of considering both when assessing the performance and reliability of computational frameworks in hypoelasticity. Computational performance is also strongly influenced by the linear solver. While multiple sub-integration steps improve accuracy, minimizing the number of global Newton iterations remains crucial to reduce overall cost. The higher computational cost observed for the Green-Naghdi and Logarithmic rates stems from the spectral decomposition required to evaluate their respective spin tensors. While the Jaumann rate is computed directly from the velocity gradient, these rates necessitate the extraction of the principal stretches. The current implementation recomputes these quantities at each sub-iteration; however, the computational cost

could be mitigated in future iterations of the framework by adopting optimized spectral algorithms or incremental update schemes for the rotation and stretch tensors. While the present study uses a fixed number of sub-steps to evaluate the framework's baseline accuracy, we acknowledge that an adaptive sub-stepping strategy would be more efficient for complex loading histories. Such an approach, which we aim to explore in future work, would involve monitoring a local criterion – such as the rate of change of the stress tensor or a local error estimate – and dynamically adjusting the sub-step size to meet a prescribed tolerance. This would ensure optimal computational efficiency without compromising the numerical integrity of the stress integration.

At this stage, it is important to distinguish the reference-frame integration used here from alternative co-rotational integration algorithms. In the latter, the objective rate is converted into a material time rate within a rotating coordinate system defined by a specific spin tensor [15, 21, 34]. While such algorithms are highly effective, particularly within Updated Lagrangian frameworks, the present study adopts a Total Lagrangian perspective. This choice ensures a unified benchmark for different rates by performing the *pull-back* operation to the fixed reference configuration, maintaining kinematic and energetic consistency with the global equilibrium equations without requiring incremental frame updates at each sub-stepping stage.

The framework is tested through three benchmark problems of increasing complexity: (i) a single-element material point simulation, (ii) a plate with a central hole under planar loading and (iii) a Cook Membrane subjected to a mixed in-plane and out-of-plane shear load. These tests confirm that classical objective stress rates such as Jaumann and Green-Naghdi are not integrable, leading to the accumulation of residual stresses and spurious energy under cyclic loading. In contrast, the logarithmic stress rate, which is integrable for grade-zero hypoelasticity, results in significantly lower residual stresses. Moreover, we also demonstrate that the accuracy of the numerical integration scheme is as critical as the choice of stress rate. For instance, applying a forward Euler scheme to the logarithmic stress rate introduces errors comparable to those of non-integrable formulations. Residual stresses associated with the Jaumann rate become particularly severe at large shear strains and during asymmetric cyclic loading, but numerical artifacts are present even in simpler problems. These findings emphasize the central role of both the constitutive model and the integration strategy in ensuring reliable predictions of hypoelastic behavior.

A limitation of the present framework must also be acknowledged, as the formulation has been developed for finite strain elasticity and does not account for plasticity. When plastic deformations are introduced, the stress-free reference configuration evolves with time and as shown by [22, 23], the logarithmic stress rate ceases to be integrable. In such cases, the kinetic logarithmic rate proposed in these works must be adopted to preserve consistency. Extending the present methodology to incorporate plasticity and rigorously assessing the performance of the kinetic logarithmic rate within boundary value problems, represents an important direction for future research. Furthermore, the present numerical framework employs a purely displacement-based formulation. While sufficient for the moderately compressible materials ($\nu = 0.3$) investigated in this study, it is susceptible to volumetric locking as the Poisson ratio

approaches the incompressibility limit ($\nu \to 0.5$). To accurately simulate rubber-like materials or nearly incompressible soft tissues, the framework would need to be extended to incorporate mixed finite element methods or stabilization techniques – such as a penalty-based treatment of the volumetric Jacobian – to prevent the development of artificial pressure and spurious stiffening [8].

Overall, the proposed framework provides a versatile and extensible environment for systematically evaluating hypoelastic formulations under complex geometries and loading constraints. The utility of this platform is illustrated by our study of a non-constant stiffness formulation derived from a Eulerian strain energy potential. By implementing the Exponentiated Hencky energy, we demonstrated that the proposed numerical framework can successfully accommodate highly non-linear material laws. From a numerical perspective, our results show that these models remain integrable and free of spurious energy generation. While these findings suggest a viable pathway for extending hypoelasticity beyond grade-zero models, further theoretical studies are required to formally prove this integrability and provide a rigorous mathematical foundation for non-constant stiffness matrices in this context.

Declarations

Acknowledgements. B.S acknowledge that this project is funded by the Ecole Normale Supérieure Paris-Saclay through a CDSN Phd Grant. The international colaboration is also supported by the Université Franco-Italienne through the grant C2-97 of the Vinci 2023 Chapter 2 program. M.M. acknowledge that this project is partially funded by the European Union—NextGenerationEU, Mission 4 Component 1, CUP E53C24002920006 (PRIN 2022 Program, Project 2022Z24WLR, Acronym: MATERIAL) and by 'Fondo per lo sviluppo di tecnologie e applicazioni di intelligenza artificiale, blockchain e internet of things' granted by the Ministry of Enterprises and Made in Italy, CUP: B87H22006480008 (project acronym: SENSOLES, application n. FTE0000537).

During the preparation of this work, the authors utilized ChatGPT to enhance the spelling, grammar, and clarity of the abstract and contribution sections. Following the use of this tool, the authors thoroughly reviewed and edited the content as necessary and assume full responsibility for the publication's content. The authors recognize the potential benefits and limitations of using generative AI and AI-assisted technologies in research and have taken measures to ensure that the use of these technologies is transparent and ethical.

Conflict of interest. The authors declare that they have no conflict of interest.

Code availability. The Python framework developed in this study, together with example scripts for the different use-cases, is publicly available for reproducibility at: https://github.com/BastienSauty/FeniCSx-Hypoelasticity.

Author contribution. Conceptualization: Bastien Sauty, Claire Morin, Michele Marino, Stephane Avril; Methodology: Bastien Sauty; Writing - original draft preparation: Bastien Sauty; Writing - review and editing: Claire Morin, Michele Marino, Stephane Avril.

References

[1] Mašín, D.: Modelling of Soil Behaviour with Hypoplasticity: Another Approach to Soil Constitutive Modelling. Springer Series in Geomechanics and Geoengineering. Springer, Cham (2019). https://doi.org/10.1007/978-3-030-03976-9

[2] Naghdi, P.M.: A critical review of the state of finite plasticity. ZAMP Zeitschrift fur angewandte Mathematik und Physik **41**(3), 315–394 (1990) https://doi.org/10.1007/BF00959986

[3] Morin, C., Avril, S., Hellmich, C.: Non-affine fiber kinematics in arterial mechanics: A continuum micromechanical investigation. ZAMM - Journal of Applied Mathematics and Mechanics / Zeitschrift für Angewandte Mathematik und Mechanik **98**(12), 2101–2121 (2018) https://doi.org/10.1002/zamm.201700360

[4] Freed, A.D., Einstein, D.R.: Hypo-elastic model for lung parenchyma. Biomechanics and Modeling in Mechanobiology **11**(3-4), 557–573 (2012) https://doi.org/10.1007/s10237-011-0333-z

[5] Braun, A.L., Awruch, A.M.: A partitioned model for fluid–structure interaction problems using hexahedral finite elements with one-point quadrature. International Journal for Numerical Methods in Engineering **79**(5), 505–549 (2009) https://doi.org/10.1002/nme.2566

[6] Rafiee, A., Thiagarajan, K.P.: An SPH projection method for simulating fluid-hypoelastic structure interaction. Computer Methods in Applied Mechanics and Engineering **198**(33-36), 2785–2795 (2009) https://doi.org/10.1016/j.cma.2009.04.001

[7] Careglio, C., Canales, C., García Garino, C., Mirasso, A., Ponthot, J.P.: A numerical study of hypoelastic and hyperelastic large strain viscoplastic Perzyna type models. Acta Mechanica **227**(11), 3177–3190 (2016) https://doi.org/10.1007/s00707-015-1545-6

[8] Eshraghi, A., Papoulia, K.D., Jahed, H.: Eulerian Framework for Inelasticity Based on the Jaumann Rate and a Hyperelastic Constitutive Relation—Part I: Rate-Form Hyperelasticity. Journal of Applied Mechanics **80**(2), 021027 (2013) https://doi.org/10.1115/1.4007723

[9] Fiala, Z.: Objective time derivatives revised. Zeitschrift für angewandte Mathematik und Physik **71**(1), 4 (2020) https://doi.org/10.1007/s00033-019-1227-7

[10] Morin, C., Hellmich, C., Nejim, Z., Avril, S.: Fiber Rearrangement and Matrix Compression in Soft Tissues: Multiscale Hypoelasticity and Application to Tendon. Frontiers in Bioengineering and Biotechnology **9**, 725047 (2021) https://doi.org/10.3389/fbioe.2021.725047

[11] Bianchi, D., Morin, C., Badel, P.: Implementing a micromechanical model into a finite element code to simulate the mechanical and microstructural response of arteries. Biomechanics and Modeling in Mechanobiology **19**(6), 2553–2566 (2020) https://doi.org/10.1007/s10237-020-01355-y

[12] Segurado, J., Lebensohn, R.A., LLorca, J., Tomé, C.N.: Multiscale modeling of plasticity based on embedding the viscoplastic self-consistent formulation in implicit finite elements. International Journal of Plasticity **28**(1), 124–140 (2012) https://doi.org/10.1016/j.ijplas.2011.07.002

[13] Xiao, S., Sun, S.-Y., Xu, G.-K., Feng, X.-Q.: A finite-strain micromechanical model for the hyperelasticity of tendons and ligaments with crimped fibers. Mechanics of Materials **160**, 103955 (2021) https://doi.org/10.1016/j.mechmat.2021.103955

[14] Nemat-Nasser, S.: Averaging theorems in Finite deformation plasticity. Mechanics of Materials **31**(8), 493–523 (1999) https://doi.org/10.1016/S0167-6636(98)00073-8

[15] Palizi, M., Federico, S., Adeeb, S.: Consistent numerical implementation of hypoelastic constitutive models. Zeitschrift für angewandte Mathematik und Physik **71**(5), 156 (2020) https://doi.org/10.1007/s00033-020-01335-3

[16] Gambirasio, L., Chiantoni, G., Rizzi, E.: On the Consequences of the Adoption of the Zaremba–Jaumann Objective Stress Rate in FEM Codes. Archives of Computational Methods in Engineering **23**(1), 39–67 (2016) https://doi.org/10.1007/s11831-014-9130-z

[17] Bernstein, B.: Hypo-elasticity and elasticity. Archive for Rational Mechanics and Analysis **6**(1), 89–104 (1960) https://doi.org/10.1007/BF00276156

[18] Noll, W.: On the Continuity of the Solid and Fluid States. Indiana University Mathematics Journal **4**(1), 3–81 (1955) https://doi.org/10.1512/iumj.1955.4.54001

[19] Leonov, A.I.: On the conditions of potentiality in finite elasticity and hypoelasticity. International Journal of Solids and Structures **37**(18), 2565–2576 (2000) https://doi.org/10.1016/S0020-7683(99)00009-8

[20] Rajagopal, K.R., Srinivasa, A.R.: On a class of non-dissipative materials that are not hyperelastic. Proceedings of the Royal Society A: Mathematical, Physical and Engineering Sciences **465**(2102), 493–500 (2009) https://doi.org/10.1098/rspa.2008.0319

[21] Lin, R.: Numerical study of consistency of rate constitutive equations with elasticity at finite deformation. International Journal for Numerical Methods in Engineering **55**(9), 1053–1077 (2002) https://doi.org/10.1002/nme.536

[22] Jiao, Y., Fish, J.: Is an additive decomposition of a rate of deformation and objective stress rates passé? Computer Methods in Applied Mechanics and Engineering **327**, 196–225 (2017) https://doi.org/10.1016/j.cma.2017.07.021

[23] Jiao, Y., Fish, J.: On the equivalence between the multiplicative hyper-elasto-plasticity and the additive hypo-elasto-plasticity based on the modified kinetic logarithmic stress rate. Computer Methods in Applied Mechanics and Engineering **340**, 824–863 (2018) https://doi.org/10.1016/j.cma.2018.06.017

[24] Simo, J.C., Pister, K.S.: Remarks on rate constitutive equations for finite deformation problems: Computational implications. Computer Methods in Applied Mechanics and Engineering **46**(2), 201–215 (1984) https://doi.org/10.1016/0045-7825(84)90062-8

[25] Trajkovic-Milenkovic, M., Bruhns, O.: Numerical analysis of finite hypo-elastic cyclic deformation with large rotations. Facta universitatis - series: Architecture and Civil Engineering **17**(3), 299–313 (2019) https://doi.org/10.2298/FUACE190513006T

[26] Aubram, D.: Notes on rate equations in nonlinear continuum mechanics. Mathematics and Mechanics of Solids **30**(7), 1527–1589 (2025) https://doi.org/10.1177/10812865241288526

[27] Xiao, H., Bruhns, O.T., Meyers, A.: Objective stress rates, path-dependence properties and non-integrability problems. Acta Mechanica **176**(3-4), 135–151 (2005) https://doi.org/10.1007/s00707-005-0218-2

[28] Ji, W., Waas, A.M., Bažant, Z.P.: Errors Caused by Non-Work-Conjugate Stress and Strain Measures and Necessary Corrections in Finite Element Programs. Journal of Applied Mechanics **77**(4), 044504 (2010) https://doi.org/10.1115/1.4000916

[29] Bažant, Z.P., Gattu, M., Vorel, J.: Work conjugacy error in commercial finite-element codes: Its magnitude and how to compensate for it. Proceedings of the Royal Society A: Mathematical, Physical and Engineering Sciences **468**(2146), 3047–3058 (2012) https://doi.org/10.1098/rspa.2012.0167

[30] Xiao, H., Bruhns, O.T., Meyers, A.: Logarithmic strain, logarithmic spin and logarithmic rate. Acta Mechanica **124**(1-4), 89–105 (1997) https://doi.org/10.1007/BF01213020

[31] Xiao, H., Bruhns, O.T., Meyers, A.: On objective corotational rates and their defining spin tensors. International Journal of Solids and Structures **35**(30), 4001–4014 (1998) https://doi.org/10.1016/S0020-7683(97)00267-9

[32] Xiao, H., Bruhns, O.T., Meyers, A.: Existence and uniqueness of the integrable-exactly hypoelastic equation $\overset{\circ}{\boldsymbol{\tau}} = \lambda(\mathrm{tr}\mathbf{D})\mathbf{I} + 2\mu\mathbf{D}$ and its significance to finite

inelasticity. Acta Mechanica **138**(1-2), 31–50 (1999) https://doi.org/10.1007/BF01179540

[33] Zhou, X., Tamma, K.K.: On the applicability and stress update formulations for corotational stress rate hypoelasticity constitutive models. Finite Elements in Analysis and Design **39**(8), 783–816 (2003) https://doi.org/10.1016/S0168-874X(03)00059-3

[34] Lim, J., Salgado, R., Prezzi, M.: Stress integration scheme for coupled elasto-plastic materials in a hypoelasto-plastic framework. International Journal of Solids and Structures **265–266**, 112121 (2023) https://doi.org/10.1016/j.ijsolstr.2023.112121

[35] Wang, S., Wu, W., Peng, C., He, X., Cui, D.: Numerical integration and FE implementation of a hypoplastic constitutive model. Acta Geotechnica **13**(6), 1265–1281 (2018) https://doi.org/10.1007/s11440-018-0684-z

[36] Sussman, T., Bathe, K.-J.: A finite element formulation for nonlinear incompressible elastic and inelastic analysis. Computers & Structures **26**(1-2), 357–409 (1987) https://doi.org/10.1016/0045-7949(87)90265-3

[37] Bathe, K.-J. (ed.): Finite Element Procedures, 2nd edition edn. K.J. Bathe, Watertown, MA (2014)

[38] Léger, S., Fortin, A., Tibirna, C., Fortin, M.: An updated Lagrangian method with error estimation and adaptive remeshing for very large deformation elasticity problems. International Journal for Numerical Methods in Engineering **100**(13), 1006–1030 (2014) https://doi.org/10.1002/nme.4786

[39] Wang, M., Panicaud, B., Rouhaud, E., Kerner, R., Roos, A.: Incremental constitutive models for elastoplastic materials undergoing finite deformations by using a four-dimensional formalism. International Journal of Engineering Science **106**, 199–219 (2016) https://doi.org/10.1016/j.ijengsci.2016.06.006

[40] Panicaud, B., Rouhaud, E., Altmeyer, G., Wang, M., Kerner, R., Roos, A., Ameline, O.: Consistent hypo-elastic behavior using the four-dimensional formalism of differential geometry. Acta Mechanica **227**(3), 651–675 (2016) https://doi.org/10.1007/s00707-015-1470-8

[41] Kolev, B., Desmorat, R.: Objective Rates as Covariant Derivatives on the Manifold of Riemannian Metrics. arXiv (2021)

[42] Pinsky, P.M., Ortiz, M., Pister, K.S.: Numerical integration of rate constitutive equations in finite deformation analysis. Computer Methods in Applied Mechanics and Engineering **40**(2), 137–158 (1983) https://doi.org/10.1016/0045-7825(83)90087-7

[43] Zhou, X., Sha, D., Tamma, K.K.: A novel non-linearly explicit second-order accurate L-stable methodology for finite deformation: Hypoelastic/hypoelasto-plastic structural dynamics problems. International Journal for Numerical Methods in Engineering **59**(6), 795–823 (2004) https://doi.org/10.1002/nme.878

[44] Alnæs, M.S., Logg, A., Ølgaard, K.B., Rognes, M.E., Wells, G.N.: Unified form language: A domain-specific language for weak formulations of partial differential equations. ACM Transactions on Mathematical Software **40**(2), 1–37 (2014) https://doi.org/10.1145/2566630

[45] Scroggs, M.W., Dokken, J.S., Richardson, C.N., Wells, G.N.: Construction of Arbitrary Order Finite Element Degree-of-Freedom Maps on Polygonal and Polyhedral Cell Meshes. ACM Transactions on Mathematical Software **48**(2), 1–23 (2022) https://doi.org/10.1145/3524456

[46] Scroggs, M.W., Baratta, I.A., Richardson, C.N., Wells, G.N.: Basix: A runtime finite element basis evaluationlibrary. Journal of Open Source Software **7**(73), 3982 (2022) https://doi.org/10.21105/joss.03982

[47] Baratta, I.A., Dean, J.P., Dokken, J.S., Habera, M., Hale, J.S., Richardson, C.N., Rognes, M.E., Scroggs, M.W., Sime, N., Wells, G.N.: DOLFINx: The next Generation FEniCS Problem Solving Environment. Zenodo (2023). https://doi.org/10.5281/ZENODO.10447666

[48] Truesdell, C.: Hypo-elasticity. Journal of Rational Mechanics and Analysis **4**, 83–1020 (1955) 24900356

[49] Xiao, H., Bruhns, O.T., Meyers, A.: A Natural Generalization of Hypoelasticity and Eulerian Rate Type Formulation of Hyperelasticity. Journal of Elasticity **56**(1), 59–93 (1999) https://doi.org/10.1023/A:1007677619913

[50] Xiao, H., Bruhns, O.T., Meyers, A.: Objective stress rates, cyclic deformation paths, and residual stress accumulation. ZAMM **86**(11), 843–855 (2006) https://doi.org/10.1002/zamm.200610276

[51] Xiao, H., Bruhns, O.T., Meyers, A.: The integrability criterion in finite elastoplasticity and its constitutive implications. Acta Mechanica **188**(3-4), 227–244 (2007) https://doi.org/10.1007/s00707-006-0362-3

[52] Neff, P., Husemann, N.J., Tchakoutio, A.S.N., Korobeynikov, S.N., Martin, R.J.: The Corotational Stability Postulate: Positive Incremental Cauchy Stress Moduli for Diagonal, Homogeneous Deformations in Isotropic Nonlinear Elasticity. arXiv (2024). https://doi.org/10.48550/arXiv.2411.12552

[53] Humphrey, J.D.: Mechanics of the arterial wall: Review and directions. Critical Reviews in Biomedical Engineering **23**(1-2), 1–162 (1995)

[54] Wang, R., Mattson, J.M., Zhang, Y.: Effect of aging on the biaxial mechanical behavior of human descending thoracic aorta: Experiments and constitutive modeling considering collagen crosslinking. Journal of the Mechanical Behavior of Biomedical Materials **140**, 105705 (2023) https://doi.org/10.1016/j.jmbbm.2023.105705

[55] Xiao, H.: Hencky Strain and Hencky Model: Extending History and Ongoing Tradition. Multidiscipline Modeling in Materials and Structures **1**(1), 1–52 (2005) https://doi.org/10.1163/1573611054455148

[56] Wriggers, P.: Nonlinear Finite Element Methods. Springer, Berlin Heidelberg (2008)

[57] Hoger, A.: The stress conjugate to logarithmic strain. International Journal of Solids and Structures **23**(12), 1645–1656 (1987) https://doi.org/10.1016/0020-7683(87)90115-6

[58] Atluri, S.N.: On constitutive relations at finite strain: Hypo-elasticity and elasto-plasticity with isotropic or kinematic hardening. Computer Methods in Applied Mechanics and Engineering **43**(2), 137–171 (1984) https://doi.org/10.1016/0045-7825(84)90002-1

[59] Nazem, M., Carter, J.P., Sheng, D., Sloan, S.W.: Alternative stress-integration schemes for large-deformation problems of solid mechanics. Finite Elements in Analysis and Design **45**(12), 934–943 (2009) https://doi.org/10.1016/j.finel.2009.09.006

[60] Raza, S.H., Soyarslan, C., Bargmann, S., Klusemann, B.: Computational modeling of amorphous polymers: A Lagrangian logarithmic strain space formulation of a glass–rubber constitutive model. Computer Methods in Applied Mechanics and Engineering **344**, 887–909 (2019) https://doi.org/10.1016/j.cma.2018.10.007

[61] Hughes, T.J.R., Winget, J.: Finite rotation effects in numerical integration of rate constitutive equations arising in large-deformation analysis. International Journal for Numerical Methods in Engineering **15**(12), 1862–1867 (1980) https://doi.org/10.1002/nme.1620151210